Olivine composition and reflectance spectroscopy relationship revisited from advanced MGM deconvolution based on synthetic and natural samples

P.C. C Pinet, Y.H. H Daydou, S.D. D Chevrel

Icarus 373 (2022) 114765

Contents lists available at ScienceDirect

Icarus

journal homepage: www.elsevier.com/locate/icarus

Olivine composition and reflectance spectroscopy relationship revisited from advanced MGM deconvolution based on synthetic and natural samples

P.C. Pinet [a,b,*], Y.H. Daydou [a,b], S.D. Chevrel [a,b]

[a] Université de Toulouse, UPS-OMP, IRAP, Toulouse, France
[b] CNRS/CNES, IRAP, 14, avenue Edouard Belin, F-31400 Toulouse, France

ARTICLE INFO

Keywords:
Spectroscopy
Mineralogy
Data reduction techniques
Olivine samples
Moon, surface

ABSTRACT

The behavior of the three primary olivine absorptions near 1 μm (referred to as M1-1, M2, M1-2) is revisited by means of an advanced version of MGM analysis. The (M1-1, M2, M1-2) band center positions are used simultaneously to produce a constrained prediction across an extended range Fo#[0–90] of olivine solid solution composition. The established trend lines based on synthetic samples from the Suny and Bristol suites appear robust when implemented on natural samples, and represent an improvement over previous solutions. The methodology, based on a wavelength deconvolution along the entire visible and near-infrared range (540-2600 nm), and the trend lines derived from the current solution, perform well, even when considering the complex situation of chromite-bearing lunar olivines. Furthermore, through the use of separate and quadratic estimates to the trends, an assessment is offered to qualify the Fo# determination made on unknown samples and/or remote sensing observations.

1. Introduction

Over the last decades, considerable effort has been put on the modeling of the composite olivine absorption feature near 1 μm classically used for determining the olivine composition from optical remote sensing measurements in the visible - near-infrared domain.

Beyond seminal works (e.g., Burns, 1970; Clark and Roush, 1984; King and Ridley, 1987; Sunshine and Pieters, 1998), a number of recent studies (e.g., Dyar et al., 2009; Clenet et al., 2011; Isaacson et al., 2014; Serventi et al., 2015; Pinet et al., 2016) have led to significant improvements on several aspects of this multifaceted problem.

On the one hand, while Sunshine and Pieters (1998) initially worked on a suite of natural olivine samples, further investigation has revealed that these samples might be influenced by the presence of minor impurities which could contribute to spectroscopic modulations of the considered spectra and disturb the intrinsic olivine Fe $^{2+}$ absorptions, leading to possible biases in the subsequent analyses of the spectral behavior of the M1-1, M2 and M1-2 bands. This has motivated the careful preparation and selection of 'pure' synthetic samples in view of assessing the quality / robustness of the regression trend lines defined for the full forsterite-fayalite solid solution series (e.g., Dyar et al., 2009, Isaacson et al., 2014, …).

On the other hand, a lot of progress has been made with the use of the Modified Gaussian Model (MGM) to address the non-linear deconvolution of visible-infrared spectra, including the cases of complex mineralogical assemblages (e.g., Noble et al., 2006; Pompilio et al., 2009; Clenet et al., 2011; Parente et al., 2011; Verpoorter et al., 2014; Serventi et al., 2015; Serventi et al., 2016; Pinet et al., 2016; Li et al., 2019, …). The recent evolution in planetary surface exploration toward thermal and crossover mid-infrared investigations (e.g., Hamilton and Christensen, 2005; Koeppen and Hamilton, 2008; Hamilton, 2010; Lane et al., 2011; Kremer et al., 2020) is promising, but it still remains that the characterization of the olivine composition variation from visible near-infrared spectroscopy has not yet been fully worked out despite significant implications.

Accordingly, we revisit here the behavior of the three primary olivine absorptions near 1 μm (referred to as M1-1, M2, M1-2) and their interelationships by means of an advanced version of MGM analysis (Pinet et al., 2019). We build on the works previously carried out (e.g., Sunshine and Pieters, 1998; Isaacson et al., 2014; Han et al., 2020) to characterize at best the compositional variation of olivine from diagnostic absorption features across the visible and near-infrared wavelengths due to electronic transitions of Fe2+ in the crystal structure.

* Corresponding author at: IRAP/UMR5277, Observatoire Midi-Pyrénées, 14, Avenue Edouard Belin, 31400, Toulouse, France.
E-mail address: patrick.pinet@irap.omp.eu (P.C. Pinet).

https://doi.org/10.1016/j.icarus.2021.114765
Received 10 June 2021; Received in revised form 8 October 2021; Accepted 19 October 2021
Available online 28 October 2021

Table 1
Description of the L4, L5, L6, L7 configurations implemented, with the characteristics (parameters and uncertainties) of the Gaussians used to initialize the MGM modeling. "✓"in the column means that the Gaussian is used in the corresponding configuration.

Gaussian	*L4*	***L5***	*L6*	*L7*	*Center (nm)*	*Width (nm)*	*Intensity*
"450"	✓	✓	✓	✓	450 ± 300	500 ± 1000	−0.25 ± 0.5
"650"		✓	✓	✓	650 ± 150	150 ± 300	−0.25 ± 0.5
M1–1	✓	✓	✓	✓	850 ± 200	250 ± 500	−0.25 ± 0.5
M2	✓	✓	✓	✓	1050 ± 200	200 ± 500	−0.25 ± 0.5
M1–2	✓	✓	✓	✓	1250 ± 200	450 ± 500	−0.25 ± 0.5
"2000"			✓	✓	2000 ± 400	550 ± 500	−0.25 ± 0.5
"2450"				✓	2450 ± 400	550 ± 1000	−0.25 ± 1.0

2. MGM implementation and olivine spectra deconvolution

2.1. The model

The principle of the Modified Gaussian Model is to deconvolve overlapping absorptions of mafic mineral spectra into their fundamental absorption components. Its specific interest is to directly account for electronic transition processes (e.g., Sunshine et al., 1990; Klima et al., 2007). The MGM approach is in essence able to achieve a direct detection and quantification of minerals. It is achieved by considering a sum of modified Gaussian functions characterized by their band centers, widths, and intensities. Spectra are modeled in the logarithm of reflectance space as a sum of modified Gaussian distributions superimposed on a baseline continuum. The resulting combinations of Gaussians can then be interpreted in terms of mineralogy. However, as demonstrated (see Kanner et al., 2007; Clenet et al., 2011), MGM results are sensitive to the initial parameters (i.e., centers, widths, and intensities) and a key issue is to properly initialize the MGM parameters (Clenet et al., 2011). Consequently, an automatic analysis of the shape of the spectrum is first performed (spectrum maxima and minima are used to estimate at first order absorption strengths and widths).

2.2. Continuum removal

It is of particular relevance to define a continuum close to the spectrum global shape in order to best isolate the absorbing features at all wavelength. However, the physical significance of the continuum is not thoroughly understood yet. In particular, its slope is influenced by the space weathering, the considered viewing geometry, the grain size of the samples, the surface texture, and the temperature. Different alternatives have been considered in the past for its removal (flat line continuum, oblique line continuum, second-order polynomial curve, energy-wavelength polynomial continuum) (e.g., Clark and Roush, 1984; Sunshine and Pieters, 1998; Noble et al., 2006; Clenet et al., 2011; Li et al., 2019; Han et al., 2020). Depending on the chosen type of continuum, the MGM results may differ, particularly, in the determination of the Gaussians band center and band depth.

In the following, at the difference of a number of previous studies, the implemented MGM approach is intended to model laboratory as well as natural rock spectra; the continuum is handled with a second-order polynomial calculated in the log reflectance / wavelength domain and initially adjusted on the local maxima along the reflectance spectrum, with its curvature, slope, and shift in reflectance free to move during the modeling (see Clenet et al., 2011). The coefficients of the polynomial are set so that the starting continuum is defined as a smooth mathematical function which is constrained by the main maxima detected along the spectrum and used as anchor points, but the final continuum (after running the MGM) may not be necessarily tangential to the spectrum. The advantage is that its overall shape is not controlled by a restricted spectral range. This is achieved by means of three anchor points searched within three spectral windows respectively spanning the intervals: 550–850, 1200–2000, 2300–2600 nm. These intervals have been defined based on an assessment of a large number of spectra for which the olivine phase is present, but may be associated with other mineral phases (e.g., Pinet et al., 2016; Pinet et al., 2018; Pinet et al., 2019). This way the continuum is handled with an approach which is close to the convex hull one but is more flexible in the sense that it does not constrain the continuum to be tangential to the spectrum. The robustness of modeling is also significantly increased with a fixed set of starting conditions able to address situations ranging from laboratory to orbital data (Clenet et al., 2011; Clenet et al., 2013; Pinet et al., 2018).

2.3. Model configuration

For the olivine MGM modeling, a set of 5 dedicated Gaussians (band center, band width, intensity and associated uncertainties) is preferentially used and referred to in the following as L5 reference configuration. The first Gaussian, centered around 450 nm, is used to model the strong large absorption at shorter wavelength (i.e. charge transfer in ultraviolet).The '650 nm' Gaussian, though generally quite shallow, appears to handle absorptions possibly caused by transitions of minor elements such as Cr, Ni or other charge transfers. Both Gaussians also contribute stabilizing the overall shape of the continuum in the visible domain. The next Gaussians respectively centered at 850, 1050, 1250 nm and referred to as M1-1, M2, M1-2 address Fe^{2+} charge transfers absorptions.

While the L5 configuration performs well for most of the spectra investigated, 3 additional configurations (L4, L6, L7) are also considered (see Table 1) and discussed in the following. These configurations will either not use the '650' Gaussian (L4) or add one or two Gaussians (L6, L7), centered at 2000 and 2450 nm to model absorption features around 2 μm which could reflect minor contaminations (H2O/OH or minor pyroxene) or spinel / glass contributions. Examples will be further given. The '2450' Gaussian may also contribute to stabilize the overall continuum shape in the near-infrared as it reduces the possible edge effect of the spectral cut-off at 2600 nm.

2.4. Methodology

Earlier efforts to establish in the visible – near infrared domain olivine absorption characteristics as a function of composition have been mainly based on natural samples (Sunshine and Pieters, 1998). However, it is recognized that natural samples are rarely representative of stoichiometric olivine of precise compositions, due to the presence of minor amounts of non-stochiometric cations such as Fe^{3+}, Cr^{2+}, Ca^{2+}, … Building on the work from Isaacson et al. (2014), this has prompted the present investigation based on well-characterized synthetic samples (Dyar et al., 2009), with the strategy of exploring through a systematic numerical testing whether there were (or not) implications when removing synthetic samples on which there could be some doubt, and to confront the results with those drawn from previous studies, largely based on natural samples.

3. Revisiting the spectral analysis of laboratory samples

Following Dyar et al. (2009) and Isaacson et al. (2014), it appears that natural olivine samples tend to exhibit greater compositional variability than synthetic ones. Grains size may also affect the chemical characterization (e.g. Crown and Pieters, 1987; Mustard and Hays, 1997; Lucey, 1998). It has been shown (Clenet et al., 2011) that large grains forsterite samples have absorption characteristics that may mimic fayalite absorption features. This effect appears when the grains size exceeds 250 μm and for grains larger than 1 mm, approaching the case of rock slab, saturation may be reached (e.g., Pompilio et al., 2009). Indeed, large particle size and textural effects contribute to the observed broad 1 μm band absorptions and this must be kept in mind when analyzing large hyperspectral datasets such as the ones produced for the martian surface with OMEGA and CRISM (e.g., Poulet et al., 2007;

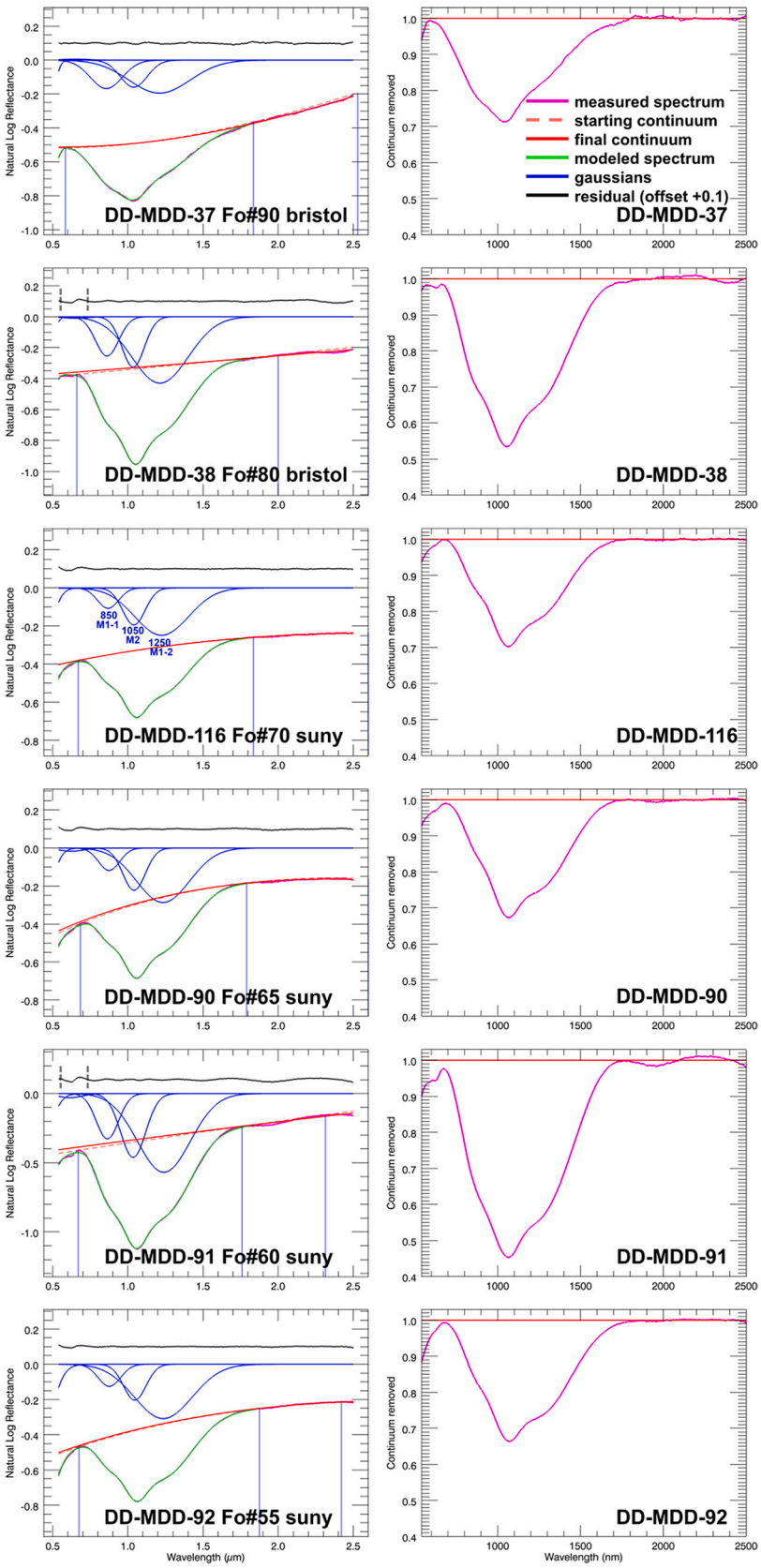

Fig. 1. *Left.* MGM deconvolution of a selection of 12 spectra (see Table 5; RELAB sample ID convention used http://www.planetary.brown.edu/relab/) spanning the forsterite-fayalite solid solution range from Fo#90 to Fo#0. Measured spectrum (pink line) and MGM modeled one (green solid line) with the Gaussians (solid blue lines) and polynomial (dashed -starting continuum- and solid -final continuum after running MGM- red lines) and the residuals line in black along the spectral domain with oscillations highlighted between vertical dashed lines for DD-MDD-38, −91, −96, −97). For clarity, the residuals (observed - modeled quantity) are shifted by +0.1 which means that a perfect fit is displayed with a 0.1 flat line. Position of the local maxima (anchor points) along the spectrum used for the process of initialization shown by thin vertical blue lines (3rd anchor point not displayed if beyond 2.5 μm). *Right.* Corresponding spectrum shown in pink after polynomial final continuum removal (red line). Spectrum DD-MDD-116 is chosen to show an example of very (Burns, 1970; Kremer et al., 2020) well-behaved deconvolution. (For interpretation of the references to colour in this figure legend, the reader is referred to the web version of this article.)

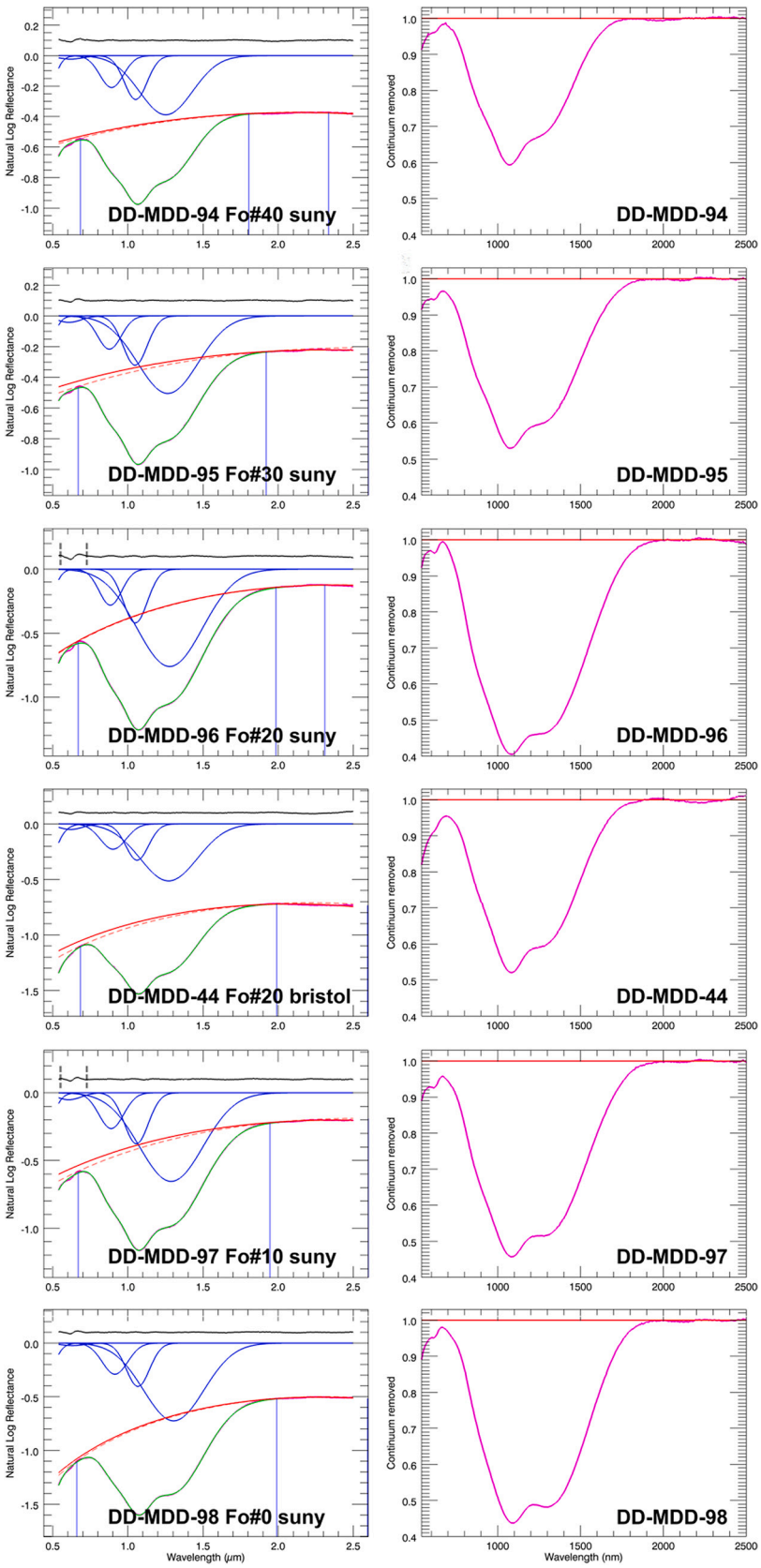

Fig. 1. (*continued*).

Table 2
MGM results for the full Suny Suite of 15 samples. From left to right: sample ID from RELAB spectral database, MGM used configuration, Fo# actual value, Rms: integrated MGM residuals along the entire spectral domain, M1–1, M2,M1–2 band centers, band widths, band depths.

	MGM Conf.			*Band center (nm)*				*Band width (nm)*				*Band depth*			
Name		*Fo#*	*Rms*	*650*	*850*	*1050*	*1250*	*650*	*850*	*1050*	*1250*	*650*	*850*	*1050*	*1250*
DD-MDD-86	L5	0.90	0.0026	618.3	866.2	1041.0	1225.6	186.3	153.1	160.5	298.4	−0.044	−0.014	−0.075	−0.054
DD-MDD-115	L5	0.90	0.0026	637.7	873.4	1038.4	1218.2	197.5	167.6	165.0	363.2	−0.009	−0.060	−0.135	−0.133
DD-MDD-87	L5	0.80	0.0034	618.4	884.9	1043.4	1226.8	185.5	169.9	162.2	378.6	−0.027	−0.069	−0.171	−0.200
DD-MDD-88	L4	0.75	0.0028	–	878.1	1042.5	1219.5	–	157.5	169.2	408.5	–	−0.064	−0.142	−0.165
DD-MDD-89	L4	0.70	0.0020	–	881.1	1050.5	1227.7	–	198.4	170.2	431.6	–	−0.108	−0.161	−0.223
DD-MDD-116	L5	0.70	0.0024	644.1	868.8	1040.0	1225.0	199.8	165.3	175.3	420.2	−0.002	−0.107	−0.195	−0.249
DD-MDD-90	L5	0.65	0.0030	624.0	875.4	1041.5	1234.5	195.3	165.0	176.4	414.2	−0.017	−0.118	−0.223	−0.287
DD-MDD-91	L5	0.60	0.0074	614.4	864.1	1035.4	1239.8	192.9	174.5	195.8	413.3	−0.030	−0.327	−0.461	−0.569
DD-MDD-92	L5	0.55	0.0021	644.7	876.9	1045.9	1236.0	199.4	174.4	175.0	450.7	−0.001	−0.126	−0.204	−0.308
DD-MDD-93	L5	0.50	0.0025	619.8	881.9	1046.3	1232.5	193.1	161.7	173.0	421.5	−0.015	−0.098	−0.185	−0.228
DD-MDD-94	L5	0.40	0.0030	620.0	892.1	1052.5	1253.4	194.5	183.9	177.2	414.5	−0.023	−0.209	−0.288	−0.388
DD-MDD-95	L5	0.30	0.0027	608.7	877.6	1048.6	1266.3	193.3	183.9	188.4	473.5	−0.042	−0.217	−0.321	−0.504
DD-MDD-96	L5	0.20	0.0049	655.4	884.1	1050.0	1278.7	200.0	176.1	187.4	513.0	0.000	−0.281	−0.420	−0.760
DD-MDD-97	L5	0.10	0.0030	607.5	889.5	1056.8	1288.7	190.9	193.3	186.6	498.6	−0.052	−0.264	−0.377	−0.655
DD-MDD-98	L5	0.00	0.0032	633.1	914.3	1067.2	1305.1	197.4	199.0	180.9	471.1	−0.023	−0.290	−0.404	−0.724

Table 3
MGM results for the full Bristol Suite of 10 samples. From left to right: sample ID from RELAB spectral database, MGM used configuration, Fo# actual value, Rms: integrated MGM residuals along the entire spectral domain, M1-1, M2, M1-2 band centers, band widths, band depths.

	MGM Conf.			*Band center (nm)*				*Band width (nm)*				*Band depth*			
Name		*Fo#*	*Rms*	*650*	*850*	*1050*	*1250*	*650*	*850*	*1050*	*1250*	*650*	*850*	*1050*	*1250*
DD-MDD-37	L5	0.90	0.0035	650.4	857.0	1039.6	1211.2	200.1	248.8	209.0	478.5	0.006	−0.168	−0.160	−0.195
DD-MDD-38	L5	0.80	0.0047	648.6	861.8	1035.3	1213.8	200.4	180.5	175.5	442.0	−0.010	−0.254	−0.326	−0.430
DD-MDD-39	L4	0.70	0.0064	–	852.4	1032.3	1232.9	–	168.1	190.0	489.9	–	−0.298	−0.425	−0.663
DD-MDD-40	L5	0.60	0.0043	640.8	908.1	1053.0	1236.3	198.8	181.5	161.6	405.9	−0.006	−0.159	−0.258	−0.368
DD-MDD-41	L4	0.50	0.0049	–	869.1	1045.2	1252.8	–	189.3	190.9	464.5	–	−0.358	−0.467	−0.706
DD-MDD-42	L5	0.40	0.0049	657.8	875.1	1046.9	1263.6	199.1	184.8	192.6	473.2	0.006	−0.372	−0.514	−0.821
DD-MDD-43	L5	0.30	0.0031	653.5	916.4	1064.9	1284.1	193.8	204.6	177.0	445.2	−0.077	−0.237	−0.339	−0.621
DD-MDD-44	L5	0.20	0.0037	618.9	902.4	1061.8	1271.9	190.1	200.0	176.3	447.8	−0.050	−0.228	−0.327	−0.514
DD-MDD-45	L5	0.10	0.0042	628.9	915.0	1069.0	1290.5	191.9	216.1	173.5	431.4	−0.043	−0.211	−0.289	−0.456
DD-MDD-46	L5	0.00	0.0060	641.6	887.5	1055.4	1319.4	177.9	292.3	202.0	409.5	−0.122	−0.084	−0.212	−0.303

Poulet et al., 2009; Clenet et al., 2013; Ody et al., 2013; Brown et al., 2020). Accordingly, the focus should be first put on synthetic small grain size samples.

3.1. Synthetic olivine samples

Two suites of synthetic olivine samples, with small grain sizes (<45 μm), are available and span the full range of stoichiometric olivine composition along the forsterite-fayalite solid solution series. The first suite synthesized by Donald Lindsey at Stony Brook is referred to as 'SUNY' (for State University of New York) and comprises 15 samples. The second suite is composed of 10 samples, was prepared by Richard Brooker at Bristol University and is referred to as 'BRISTOL' olivines. From a very careful characterization (Dyar et al., 2009), based on a variety of experimental analyses (Mossbauer, Raman, RELAB spectroscopy, ATR, Mid-Infrared thermal emission), BRISTOL samples, produced from incompletely reacted olivines, were found to be more subject to residual impurities than SUNY samples, which could affect their spectroscopic properties.

A first logical step is to implement our MGM deconvolution on both synthetic suites. The results of the MGM modeling is given hereafter for a selection of 12 spectra spanning the olivine composition range from Fo#90 to Fo#0 (Fig. 1). The corresponding normalized spectra after continuum removal are also displayed in Fig. 1 and the modeling outputs are given in Tables 2 and 3.

All the spectra appear to be rather well modeled in terms of MGM deconvolution, with quite low residuals comprised between 0.002 and 0.007. An example of well-behaved deconvolution results is highlighted with spectrum DD-MDD-116 (see Fig. 1). One notes however that while 9 out of 15 'suny' spectra have residuals <0.0035 (Tables 2 and 3), only 2 out of 10 'bristol' spectra have such low residuals. Furthermore, for several spectra (e.g., DD-MDD-38,-91,-96,-97), despite the overall rather low residuals, oscillations along the spectral domain indicate that there may be a leftover variability not taken into account in the modeling, mainly in the 540-700 nm range (see Fig. 1), which may be associated with spin-forbidden absorptions. Here, as the model performs, one Gaussian, referred to as '650', is implemented as a trade-off to handle at first order the spectral subtleties in this domain. Additional Gaussians could be considered in principle to better separate out and describe distinct absorptions, but their initial settings may be a difficult task. Conversely, for 4 samples out of 25 (DD-MDD-39,-41 in Bristol suite; DD-MDD-88,-89 in Suny suite) (see Tables 2 and 3), the configuration L4 with no 650 nm Gaussian is used instead of L5 as the MGM modeling is improved.

Also, while spectra generally present a flat shape longward 1.6 μm (e.g., DD-MDD-116, 92, 98), one notes that for a few spectra (e.g., DD-MDD-91), the continuum removal (see Fig. 1) highlights the presence of a weak and wide absorption feature around 2 μm (already noted by Isaacson et al., 2014) which could reflect minor contaminations (H2O/OH or minor pyroxene or glass contribution). As a consequence, the final continuum (after running the MGM) appears modeled 'below' the spectrum, at the percent level, for a limited spectral domain lying between 2.15 and 2.35 μm.

Of note, the locations/positions of the anchor points used to define

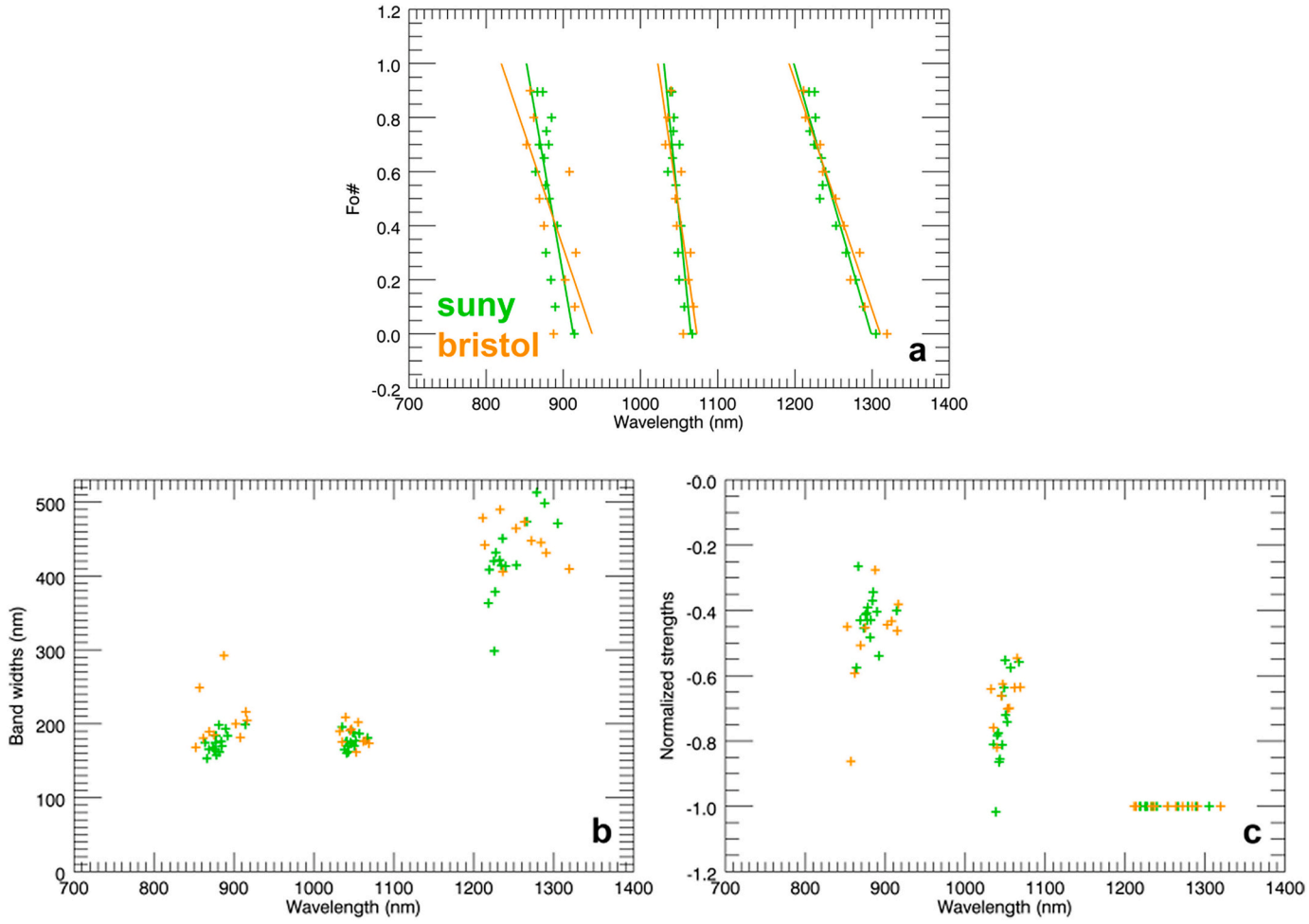

Fig. 2. (2a). Band centers from MGM deconvolution (see Tables 2 and 3) for both suites (Symbol + in orange is for "bristol" 10 synthetic samples; symbol + in green is for "suny" 15 samples). Respective regression trend lines are displayed in green (Suny) and orange (Bristol). **(2b and 2c)** Band widths and normalized strengths to M1–2 band depth. Green crosses (Suny), orange crosses (Bristol). (For interpretation of the references to colour in this figure legend, the reader is referred to the web version of this article.)

Table 4
Quadratic distances (rms) d_{850}, d_{1050}, d_{1250} to trends '850', '1050', '1250' and integrated spectral distance to trend sdt = $(1/3(d_{850})^2 + 1/3\ (d_{1050})^2 + 1/3\ (d_{1250})^2)^{1/2}$, highlighted in bold, given in nm associated with the regressions produced for Bristol and Suny suites considered separately.

RMS (considered regression)	*real distance (nm)*			
	d_{850}	d_{1050}	d_{1250}	***sdt***
RMS(Bristol)	24.4	8.3	7.4	**15.5**
RMS(Suny)	11.5	5.4	7.5	**8.5**

the overall shape of the initial polynomial continuum vary along the spectral domain within the search windows. While the position of the first anchor point is relatively stable shortward of 0.7 μm, significant changes are found for the second anchor point in the range 1.5–2.0 μm. These results highlight the difficulty of using fixed tangent points in the continuum removal process with the inherent risk of introducing a bias. After running the MGM deconvolution, the final polynomial continuum may be identical to the initial one or slightly depart from it, and may even be shifted upward in reflectance with respect to the considered spectrum as it will be shown in the following. This observation suggests that the physical significance of the continuum is not thoroughly understood yet.

The MGM outputs are given in Table 2 for the complete suny suite of 15 samples and Table 3 for the full Bristol suite of 10 samples, and the associated band centers, widths, depths are shown on Fig. 2 a,b,c.

As expected, both an increase of the Gaussian centers positions toward longer wavelengths correlated to the iron content and of the "1050"band normalized intensity are observed. However, due to the choice of a second order polynomial continuum, weaker strengths are obtained in the case of the Gaussian "850" band (i.e. between −0.4 and − 0.6) compared to the case of a flat continuum. Indeed, as noted earlier (e.g., Clenet et al., 2011; Han et al., 2020), the continuum presents a tight curvature at shorter wavelengths and thus better matches the overall shape of the spectrum than in the case of a straight line ('flat continuum'), with an effect on the relative "850" band and "1050" band strengths.

For both suites, the outputs of our MGM modeling indicate that the scattering associated with the 850 nm band center prevails over the 1050 and 1250 band centers (see Fig. 2a), as noted previously (e.g., Burns, 1993; Sunshine and Pieters, 1998). Some samples (DD-MDD-40, -46, -87, -115) (see Fig. 2a and Tables 2 and 3) markedly depart, in both suites, from the overall trends and call for caution.

While for the band widths and band depths (Fig. 2.b, c), no obvious differences are noticed between the two suites, two trends are clearly found for the band centers; with a band center scattering significantly more pronounced for the Bristol suite (see below). We also note that there are Bristol samples (DD-MDD-37,-38,-44,-45) which tend to agree with the Suny trend.

Table 5
Olivine composition estimates produced from the suite of 12 selected samples (9 Suny, 3 Bristol) (C1DD37, 38, 116, 90, 91, 92, 94, 95, 96, 44, 97, 98) which spans the olivine composition domain from Fo#0 to Fo#90. From left to right: sample ID from RELAB spectral database, MGM used configuration, Fo#: actual % molar Forsterite; Fô#: predicted % molar Forsterite, "Fô#- Fo#" (predicted-actual) is a signed quantity (+ if overestimate, − if underestimate), real distances (d_{850}, d_{1050},d_{1250}) to each M1–1, M2, M1–2 trend line, rsdt: real spectral quadratic distance to the three trends, predicted distances ($d_{850}\hat{}$, $d_{1050}\hat{}$, $d_{1250}\hat{}$) to each trend line, psdt: predicted spectral quadratic distance to the three trends. Last line 'RMS' gives the standard deviation for all quantities for the full set of samples, with rsdt ~6 nm and psdt~5 nm.

Name	*MGM Conf.*	*Fo#*	$\widehat{Fo\#}$	$\widehat{Fo\#} - Fo\#$	*real distance*				*predicted distance*			
					d_{850}	d_{1050}	d_{1250}	*rsdt*	$\widehat{d_{850}}$	$\widehat{d_{1050}}$	$\widehat{d_{1250}}$	*psdt*
DD-MDD-37	L5	0.90	0.81	−0.090	6.24	9.38	6.25	7.44	0.33	5.84	−3.17	3.84
DD-MDD-38	L5	0.80	0.79	−0.010	4.44	1.21	−1.57	2.81	3.78	0.82	−2.62	2.70
DD-MDD-116	L5	0.70	0.68	−0.020	4.88	1.97	−0.89	3.08	3.57	1.18	−2.98	2.77
DD-MDD-90	L5	0.65	0.59	−0.060	8.21	1.44	3.37	5.19	4.26	−0.91	−2.91	3.03
DD-MDD-91	L5	0.60	0.62	0.020	−6.35	−6.64	3.45	5.67	−5.04	−5.85	5.54	5.49
DD-MDD-92	L5	0.55	0.57	0.020	3.14	1.97	−5.59	3.87	4.45	2.75	−3.50	3.63
DD-MDD-94	L5	0.40	0.38	−0.020	8.45	2.64	−3.83	5.57	7.14	1.86	−5.92	5.46
DD-MDD-95	L5	0.30	0.37	0.070	−12.61	−5.21	−1.46	7.92	−8.00	−2.46	5.86	5.90
DD-MDD-96	L5	0.20	0.26	0.060	−12.65	−7.70	0.56	8.55	−8.70	−5.34	6.84	7.10
DD-MDD-44	L5	0.20	0.21	0.010	5.63	4.13	−6.32	5.44	6.29	4.53	−5.27	5.41
DD-MDD-97	L5	0.10	0.16	0.060	−13.78	−4.83	0.05	8.43	−9.84	−2.47	6.33	6.90
DD-MDD-98	L5	0.00	0.00	0.000	4.40	1.63	5.97	4.39	4.40	1.63	5.97	4.39
RMS				0.046	8.32	4.83	3.97	6.01	6.03	3.49	4.97	4.94

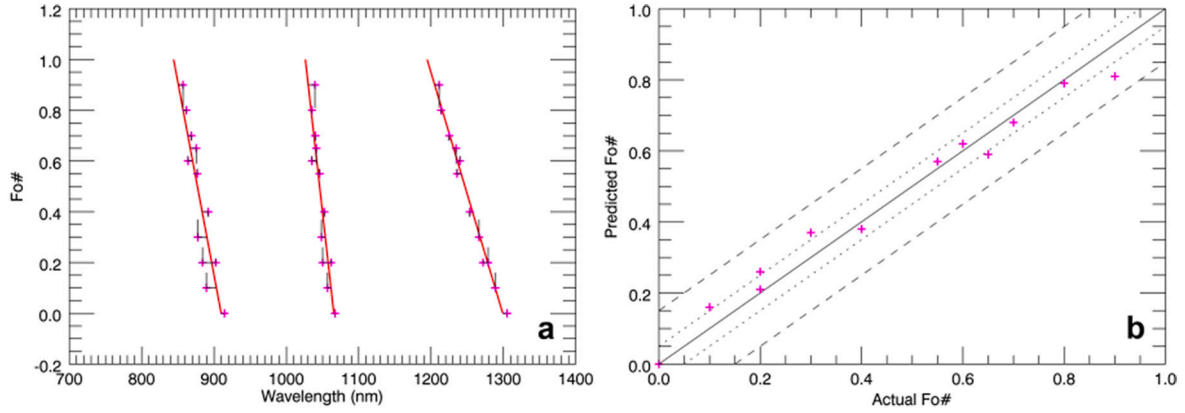

Fig. 3. (3a). Composition trend lines derived from MGM results with the 12 selected samples in Molar % Forsterite vs band center (nm) graph. Pink crosses (+) plot for each sample the actual Fo# associated with M1–1, M2, M1–2 band centers determined by MGM deconvolution (see Table 5). The horizontal thin bars display the real distances (d_{850}, d_{1050},d_{1250}) to trend lines for each sample while the vertical thin bars show the "Fô#- Fo#" (i.e., predicted-actual Fo#) quantities; **(3.b)**. Predicted (Fô#) versus Actual (Fo#) Molar % Forsterite estimates for the 12 synthetic samples from the derived trend lines shown in **3a**.

Table 6
MGM results for the Suny-Bristol suite of 19 samples. *Columns from left to right*: sample ID from RELAB spectral database (name in Italics used for the 12 samples from Table 5; * symbol (for DD-MDD-37, 90, 97) indicates the use of L6 or L7 MGM deconvolution as an improvement over the initial L5, MGM used configuration, Fo# actual value, Rms: integrated MGM residuals along the spectral domain, M1–1, M2, M1–2 band centers, band widths, band depths.

	MGM Conf.			*Band center (nm)*				*Band width (nm)*				*Band depth*			
Name		*Fo#*	*Rms*	*650*	*850*	*1050*	*1250*	*650*	*850*	*1050*	*1250*	*650*	*850*	*1050*	*1250*
*DD-MDD-37**	L7	0.90	0.0034	648.5	856.7	1039.7	1204.0	199.9	240.2	202.3	499.6	−0.003	−0.171	−0.158	−0.210
DD-MDD-38	L5	0.80	0.0047	648.6	861.8	1035.3	1213.8	200.4	180.5	175.5	442.0	−0.010	−0.254	−0.326	−0.430
DD-MDD-88	L7	0.75	0.0020	613.3	867.0	1041.0	1215.9	188.7	170.1	173.6	427.9	−0.035	−0.079	−0.146	−0.182
DD-MDD-116	L5	0.70	0.0024	644.1	868.8	1040.0	1225.0	199.8	165.3	175.3	420.2	−0.002	−0.107	−0.195	−0.249
DD-MDD-89	L7	0.70	0.0020	637.6	873.8	1049.8	1226.3	198.8	205.1	173.7	451.5	−0.020	−0.120	−0.164	−0.244
DD-MDD-39	L4	0.70	0.0064	–	852.4	1032.3	1232.9	–	168.1	190.0	489.9	–	−0.298	−0.425	−0.663
*DD-MDD-90**	L6	0.65	0.0020	610.2	871.3	1041.5	1231.4	190.2	173.9	176.4	432.1	−0.037	−0.124	−0.217	−0.299
DD-MDD-91	L5	0.60	0.0074	614.4	864.1	1035.4	1239.8	192.9	174.5	195.8	413.3	−0.030	−0.327	−0.461	−0.569
DD-MDD-92	L5	0.55	0.0021	644.7	876.9	1045.9	1236.0	199.4	174.4	175.0	450.7	−0.001	−0.126	−0.204	−0.308
DD-MDD-93	L5	0.50	0.0025	619.8	881.9	1046.3	1232.5	193.1	161.7	173.0	421.5	−0.015	−0.098	−0.185	−0.228
DD-MDD-41	L4	0.50	0.0049	–	869.1	1045.2	1252.8	–	189.3	190.9	464.5	–	−0.358	−0.467	−0.706
DD-MDD-94	L5	0.40	0.0030	620.0	892.1	1052.5	1253.4	194.5	183.9	177.2	414.5	−0.023	−0.209	−0.288	−0.388
DD-MDD-42	L5	0.40	0.0049	657.8	875.1	1046.9	1263.6	199.1	184.8	192.6	473.2	0.006	−0.372	−0.514	−0.821
DD-MDD-95	L5	0.30	0.0027	608.7	877.6	1048.6	1266.3	193.3	183.9	188.4	473.5	−0.042	−0.217	−0.321	−0.504
DD-MDD-96	L5	0.20	0.0049	655.4	884.1	1050.0	1278.7	200.0	176.1	187.4	513.0	0.000	−0.281	−0.420	−0.760
DD-MDD-44	L5	0.20	0.0037	618.9	902.4	1061.8	1271.9	190.1	200.0	176.3	447.8	−0.050	−0.228	−0.327	−0.514
*DD-MDD-97**	L7	0.10	0.0029	604.5	894.0	1060.4	1287.1	184.9	204.4	181.8	507.3	−0.061	−0.278	−0.359	−0.677
DD-MDD-45	L7	0.10	0.0026	625.7	909.8	1066.2	1285.6	190.5	211.7	170.6	465.3	−0.045	−0.200	−0.276	−0.487
DD-MDD-98	L5	0.00	0.0032	633.1	914.3	1067.2	1305.1	197.4	199.0	180.9	471.1	−0.023	−0.290	−0.404	−0.724

Table 7
Olivine composition estimates for 19 samples (12 Suny / 7 Bristol). *From left to right*: sample ID from RELAB spectral database, MGM used configuration, Fo#: actual % molar Forsterite; Fô#: predicted % molar Forsterite, "Fô#- Fo#" (predicted-actual) is a signed quantity (+ if overestimate, − if underestimate), real distances (d_{850}, d_{1050},d_{1250}) to each M1–1, M2, M1–2 trend line, rsdt: real spectral quadratic distance to the three trends, predicted distances ($d_{850}\hat{}$, $d_{1050}\hat{}$, $d_{1250}\hat{}$) to each trend line, psdt: predicted spectral quadratic distance to the three trends. Last line 'RMS' gives for the full set of samples the standard deviation for all quantities, with rsdt ~6 nm and psdt~5 nm.

Name	*MGM Conf.*	*Fo#*	$\widehat{Fo\#}$	$\widehat{Fo\#} - Fo\#$	*real distance*				*predicted distance*			
					d_{850}	d_{1050}	d_{1250}	*rsdt*	$\widehat{d_{850}}$	$\widehat{d_{1050}}$	$\widehat{d_{1250}}$	*psdt*
*DD-MDD-37**	L7	0.90	0.86	−0.040	5.92	9.47	−0.98	6.47	3.29	7.90	−5.17	5.77
DD-MDD-38	L5	0.80	0.79	−0.010	4.44	1.21	−1.57	2.81	3.78	0.82	−2.62	2.70
DD-MDD-88	L7	0.75	0.74	−0.010	6.44	4.91	−4.73	5.41	5.78	4.52	−5.78	5.39
DD-MDD-116	L5	0.70	0.68	−0.020	4.88	1.97	−0.89	3.08	3.57	1.18	−2.98	2.77
DD-MDD-89	L7	0.70	0.63	−0.070	9.88	11.72	0.43	8.85	5.28	8.97	−6.89	7.21
DD-MDD-39	L4	0.70	0.71	0.010	−11.45	−5.79	6.99	8.44	−10.80	−5.40	8.03	8.37
*DD-MDD-90**	L6	0.65	0.63	−0.020	4.09	1.50	0.30	2.52	2.77	0.72	−1.79	1.95
DD-MDD-91	L5	0.60	0.62	0.020	−6.35	−6.64	3.45	5.67	−5.04	−5.85	5.54	5.49
DD-MDD-92	L5	0.55	0.57	0.020	3.14	1.97	−5.59	3.87	4.45	2.75	−3.50	3.63
DD-MDD-93	L5	0.50	0.57	0.070	4.84	0.37	−14.32	8.73	9.44	3.12	−7.00	7.02
DD-MDD-41	L4	0.50	0.50	0.000	−7.90	−0.77	6.05	5.76	−7.90	−0.77	6.05	5.76
DD-MDD-94	L5	0.40	0.38	−0.020	8.45	2.64	−3.83	5.57	7.14	1.86	−5.92	5.46
DD-MDD-42	L5	0.40	0.40	0.000	−8.52	−3.00	6.34	6.37	−8.52	−3.00	6.34	6.37
DD-MDD-95	L5	0.30	0.37	0.070	−12.61	−5.21	−1.46	7.92	−8.00	−2.46	5.86	5.90
DD-MDD-96	L5	0.20	0.26	0.060	−12.65	−7.70	0.56	8.55	−8.70	−5.34	6.84	7.10
DD-MDD-44	L5	0.20	0.21	0.010	5.63	4.13	−6.32	5.44	6.29	4.53	−5.27	5.41
*DD-MDD-97**	L7	0.10	0.15	0.050	−9.31	−1.25	−1.54	5.49	−6.02	0.72	3.69	4.10
DD-MDD-45	L7	0.10	0.08	−0.020	6.51	4.58	−3.01	4.91	5.19	3.80	−5.10	4.74
DD-MDD-98	L5	0.00	0.00	0.000	4.40	1.63	5.97	4.39	4.40	1.63	5.97	4.39
RMS				0.036	7.76	5.06	5.15	6.12	6.51	4.18	5.52	5.49

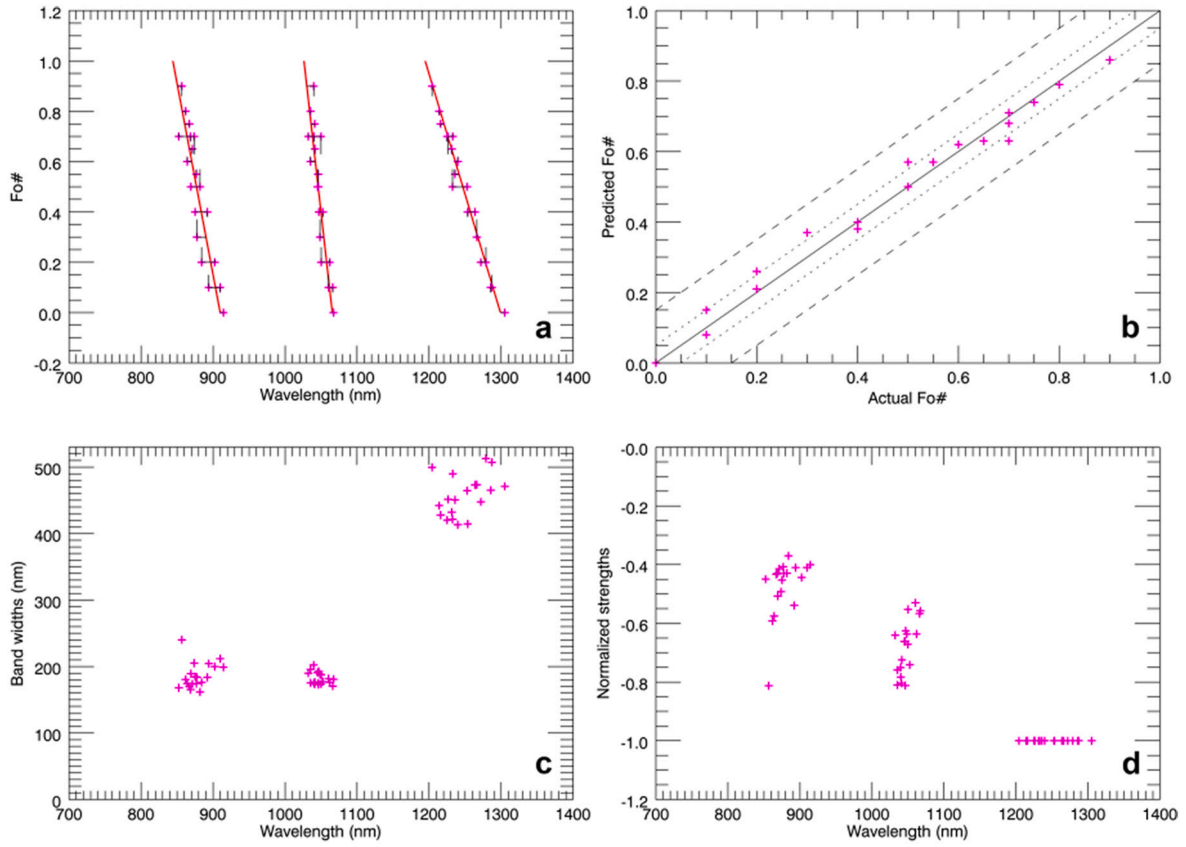

Fig. 4. (4a). MGM results with the 19 samples in Molar % Forsterite vs band center (nm) graph. Pink crosses (+) plot for each sample the actual Fo# associated with M1–1, M2, M1–2 band centers determined by MGM deconvolution (see Tables 5 and 6). The horizontal black thin bars display the real distances (d_{850}, d_{1050},d_{1250}) to trend lines for each sample while the vertical black thin bars show the "Fô# - Fo# " (i.e., predicted - actual Fo#) quantities; **(4b)**. Predicted (Fô#) versus Actual (Fo#) Molar % Forsterite estimates for the 19 synthetic samples shown in **4a**; **(4c)**. Corresponding band widths (see Table 5); **(4d).** Normalized strengths to M1–2 band from band depths (see Table 6).

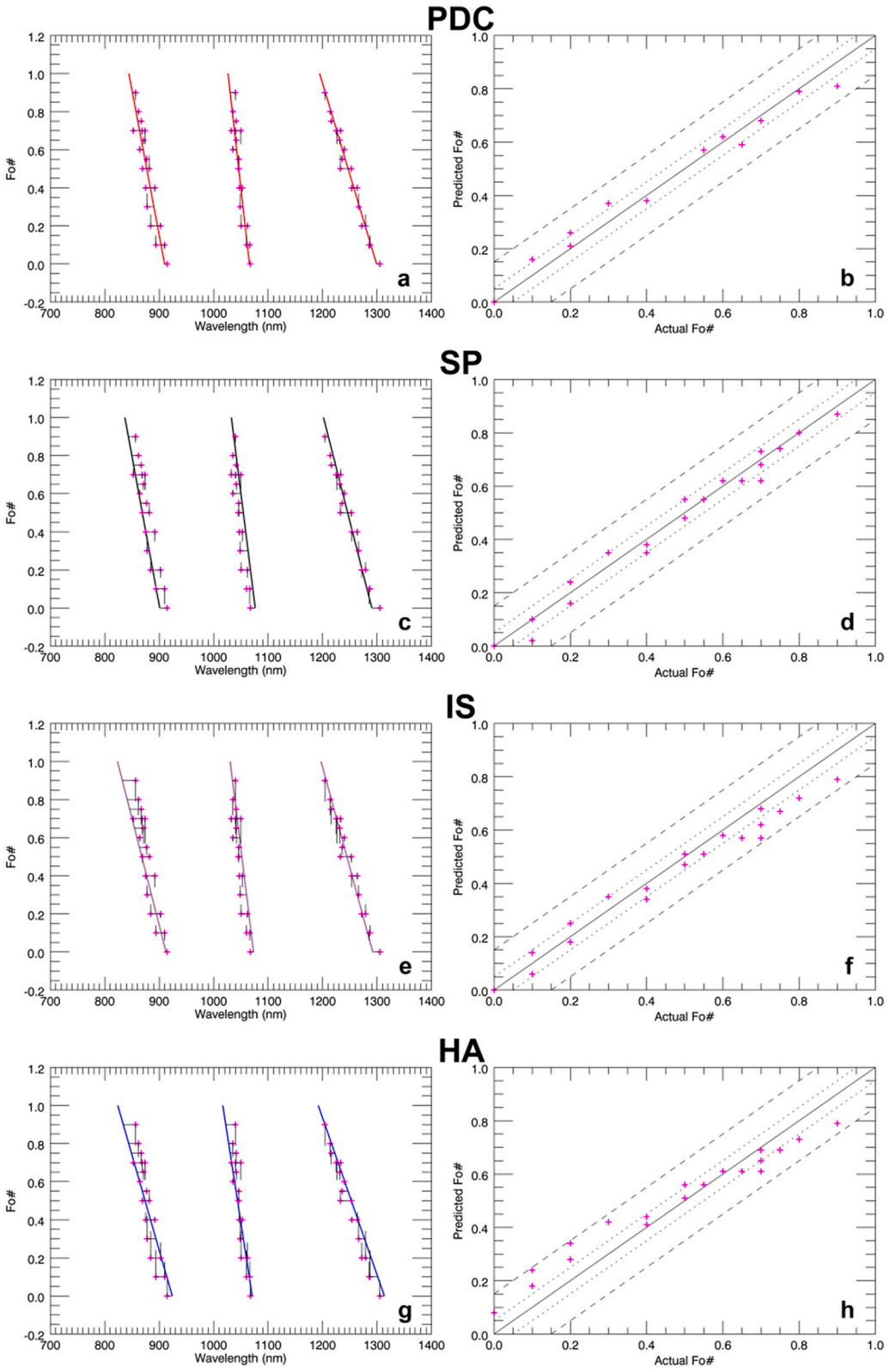

Fig. 5. *Left column:* MGM results with the 19 samples in Molar % Forsterite vs band center (nm) graph. Pink crosses (+) plot for each sample the actual Fo# associated with M1–1, M2, M1–2 band centers determined by MGM deconvolution. The horizontal black thin bars display the real distances (d_{850}, d_{1050}, d_{1250}) to trend lines for each sample while the vertical black thin bars show the "Fô#- Fo#" (i.e., predicted – actual Fo#) quantities; *Right column:* Predicted (Fô#) versus Actual (Fo#) Molar % Forsterite estimates for the 19 synthetic samples displayed on the left. (For interpretation of the references to colour in this figure legend, the reader is referred to the web version of this article.)

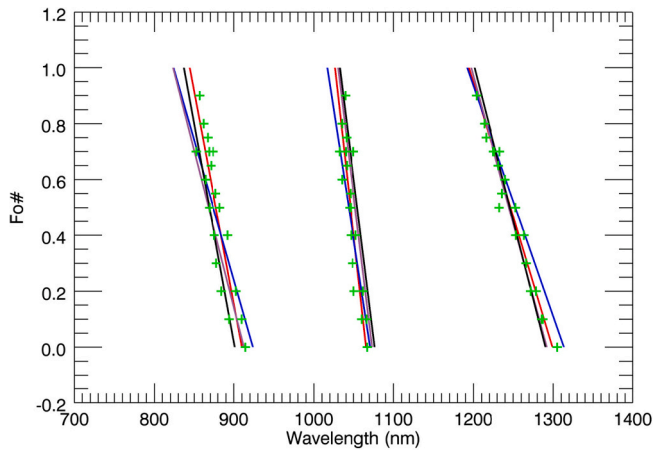

Fig. 6. Composition trend lines in Molar % Forsterite versus band center wavelength (nm) graph (in black: SP trend lines; in purple: IS trend lines from suite 1(Fo range: 0–70); in blue: HA regression (Polynomial method); in red: PDC trend lines. Green crosses + plot for each sample (Tables 6 and 7) the actual Fo# associated with M1–1, M2, M1–2 band centers determined by MGM deconvolution. (For interpretation of the references to colour in this figure legend, the reader is referred to the web version of this article.)

For both Bristol and Suny suites, band centers are used to determine trend line equations for each individual absorption band M1-1, M2, M1-2, with an assessment on the regression performance (rms spectral distance between bandcenter estimate from MGM and the one from the trend line). Quadratic distances (rms) d_{850}, d_{1050}, d_{1250} to trends '850', '1050', '1250' and integrated spectral distance to trend sdt = $(1/3\ (d_{850})^2 + 1/3\ (d_{1050})^2 + 1/3\ (d_{1250})^2)^{1/2}$, are given hereafter (see Table 4) for both Bristol and Suny suites, considered separately, and confirm the larger scattering of the '850 nm' band associated with the M1–1 absorption feature.

Based on these results, and on the previous experimental analyses mentioned above (Dyar et al., 2009), it appears that the Suny suite should be taken as the master list (ascertainment recently supported also by Kremer et al. (2020)), and possibly completed by Bristol samples to reinforce the robustness of the trend line variations as a function of composition. However, as shown above, in both suites some samples depart from the overall trend. Accordingly, a series of tests are performed on various subsets of samples selected from both Suny and Bristol suites. For each subset of considered samples, a systematic testing of the coherency is performed to assess the performance of the regression. The actual olivine composition (Molar Forsterite Fo#) is then predicted (Fô# estimate) based on minimizing the deviations in band centers from the established trends for the three absorptions simultaneously, using the integrated quadratic **s**pectral **d**istance to **t**rend quantity (**sdt**). The performance of the regression is then assessed on the basis of this quantity sdt (more precisely, rsdt: real spectral quadratic distance to trend, psdt: predicted spectral quadratic distance to trend) and on the standard deviation (rms) of the "Fô#- Fo#" quantity from Fô# estimates. It is found (see Table 5 below and Fig. 3) that the suite composed of the following twelve samples (9 Suny, 3 Bristol) (DD-MDD-37,-38,-116,-90,-91,-92,-94,-95,-96,-44,-97,-98), which entirely spans the olivine composition domain from Fo#90 to Fo#0, has the best consistency, both in terms of rsdt, psdt and Fô# estimates, with respectively an integrated standard deviation rsdt of 6 nm, psdt~5 nm and 0.046 for the "Fô#- Fo#" quantity. Clearly, this regression is significantly more robust than either the Bristol (rsdt: 15.5, psdt: 10.9, "Fo#-Fô#" (rms): 0.110) or Suny (rsdt: 8.52, psdt: 5.80, "Fo#-Fô#" (rms): 0.087) one considered separately. This way we assess and mitigate, through the statistical consistency of the considered subset, the impact of the 'poor' quality of any given sample/spectrum (e.g., Isaacson et al., 2014) in the regression set to define the trend lines equations.

Though the L5 configuration appears to be suited for the majority of the situations, it is also noted that for some spectra, the modeling can be improved (Table 6) by the addition of a couple of bands (L6 (2000nm), L7 (2000, 2450 nm)), resulting for the same previously defined regression based on L5 configuration (Table 5) in an increased consistency in terms of spectral distance to trend sdt and Fo# standard deviation estimates, respectively.

Out of the 13 other Suny or Bristol spectra not used in the regression to establish the trend lines equations, it appears that 7 of them (3 Suny: 88(L7), 89 (L7), 93(L5), 4 Bristol: 39 (L4), 41(L4), 42(L5), 45(L7)) are consistent with these regression trends (see Table 7) (rsdt<9 nm, Fô#-Fo# quantity<0.07), while (115, 86, 87, 40, 43, 46) depart from the general trend (see Fig. 2a). 46 has been shown to present problems (see Dyar et al., 2009) and 115/86 are repeated spectral measurements for the same Fo# (same sample or site?). We also suspect that 87, 40, 43 which clearly depart from both Suny and Bristol trends '850' (see Fig. 2a) may not be reliable for setting a robust regression trend due to either the occurrence of impurities, or concerns with the sample preparation or in the spectral measurements, ….

Accordingly, the 7 samples (88, 89, 93, 39, 41, 42, 45) are added to the Suny-Bristol suite which now comprises 19 samples (out of 25/24 if one considers 115 to be a repetition of 86), and the performances of coherency associated with the same regression as previously are given in Table 7.

This clearly results in an increased consistency in terms of spectral distance to trend sdt and Fo# estimates, and in band widths and band depths (displayed as normalized strengths) when compared to Fig. 2 as highlighted in Fig. 4 a,b,c,d below. One notes that the band widths of the three gaussians 850, 1050, 1250 nm are well grouped with the following respective means and standard deviations: 187 ±19 nm, 182±9 nm, 457±30 nm.

All of this confirms the robustness of the considered regression defined from synthetic samples and reinforces the confidence on the established trend lines equations established from our MGM advanced procedure, based on L5 configuration with the use of a fixed set of starting conditions.

3.2. Comparison with previous trend line equations

Given the amount of work already performed by the community in this domain, the solution currently proposed here (coined PDC for Pinet-Daydou-Chevrel) is now assessed versus previously established trend line equations from various studies. For the sake of simplicity, these previous solutions will be referred to in the following of this paper with the respective acronyms SP, (for Sunshine and Pieters, 1998); IS (for

Table 8
Synthetic Suny Bristol 19 samples. Statistical performances for the 4 compared solutions, with rms standard deviation for all quantities.

RMS (considered regression)	$\widehat{Fo\#} - Fo\#$	*real distance (nm)*				*predicted distance (nm)*			
		d_{850}	d_{1050}	d_{1250}	***rsdt***	$\widehat{d_{850}}$	$\widehat{d_{1050}}$	$\widehat{d_{1250}}$	***psdt***
RMS (PDC)	**0.036**	7.76	5.06	5.15	**6.12**	6.51	4.18	5.52	**5.49**
RMS (SP)	**0.038**	11.20	9.49	6.56	**9.28**	9.89	9.35	7.32	**8.92**
RMS (IS)	**0.061**	13.91	7.34	5.94	**9.71**	9.02	7.51	8.67	**8.42**
RMS (HA)	**0.077**	13.31	7.54	9.78	**10.49**	8.03	5.40	8.54	**7.45**

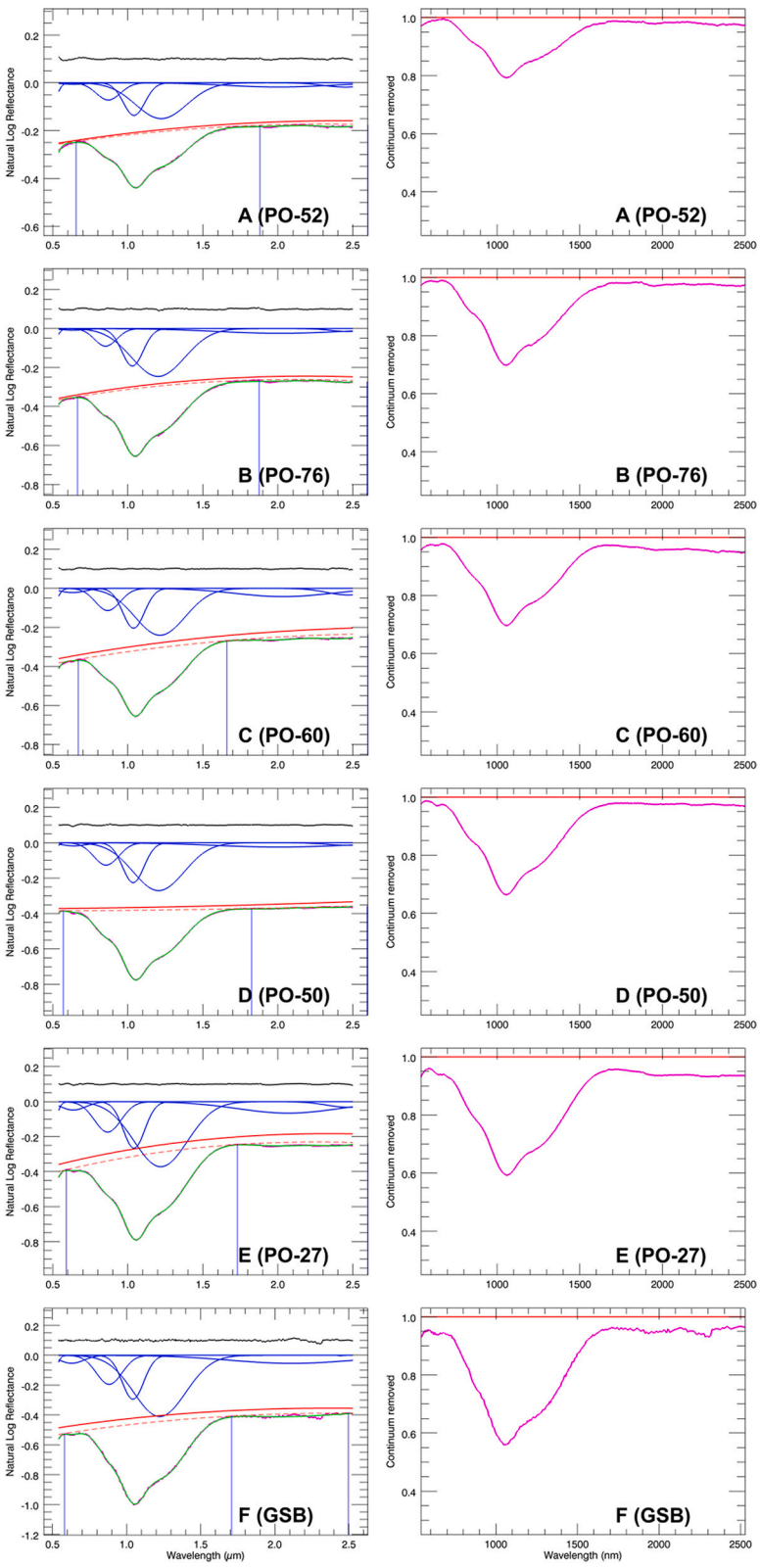

Fig. 7. *Left.* MGM deconvolution of the suite of 18 natural spectra spanning the forsterite-fayalite solid solution range from Fo#97 to Fo#0.01. Measured spectrum (pink line) and MGM modeled one (green solid line) with the Gaussians (solid blue lines) and polynomial (dashed -starting continuum- and solid -final continuum after running MGM- red lines) and the residuals line in black along the spectral domain. For clarity, the residuals (observed – modeled quantity) are shifted by +0.1 which means that a perfect fit is displayed with a 0.1 flat line. Position of the local maxima (anchor points) along the spectrum used for the process of initialization shown by thin vertical blue lines (3rd anchor point not displayed if beyond 2.5 μm). *Right.* Corresponding spectrum shown in pink after removal of the polynomial final continuum (red line). (For interpretation of the references to colour in this figure legend, the reader is referred to the web version of this article.)

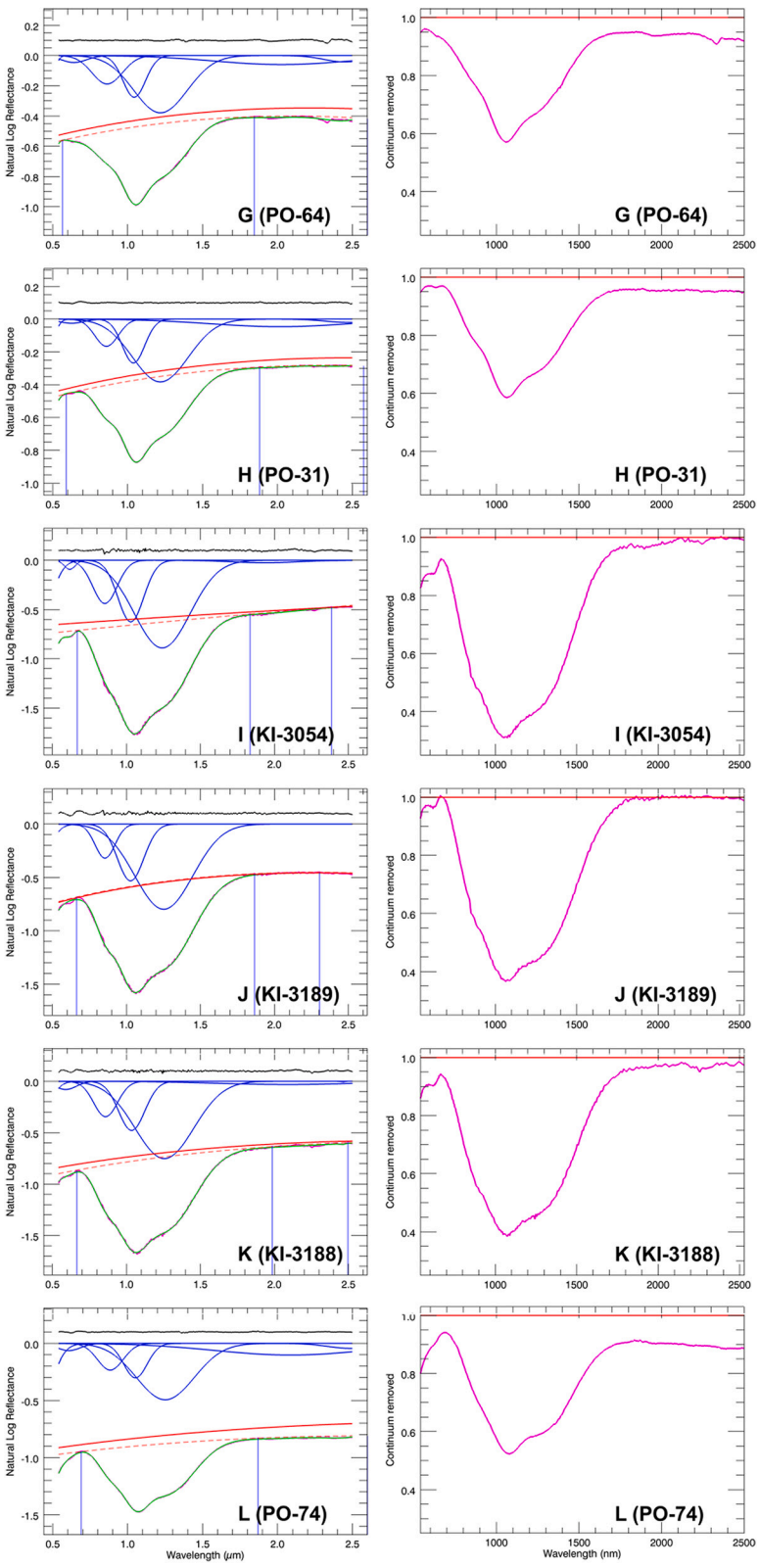

Fig. 7. (*continued*).

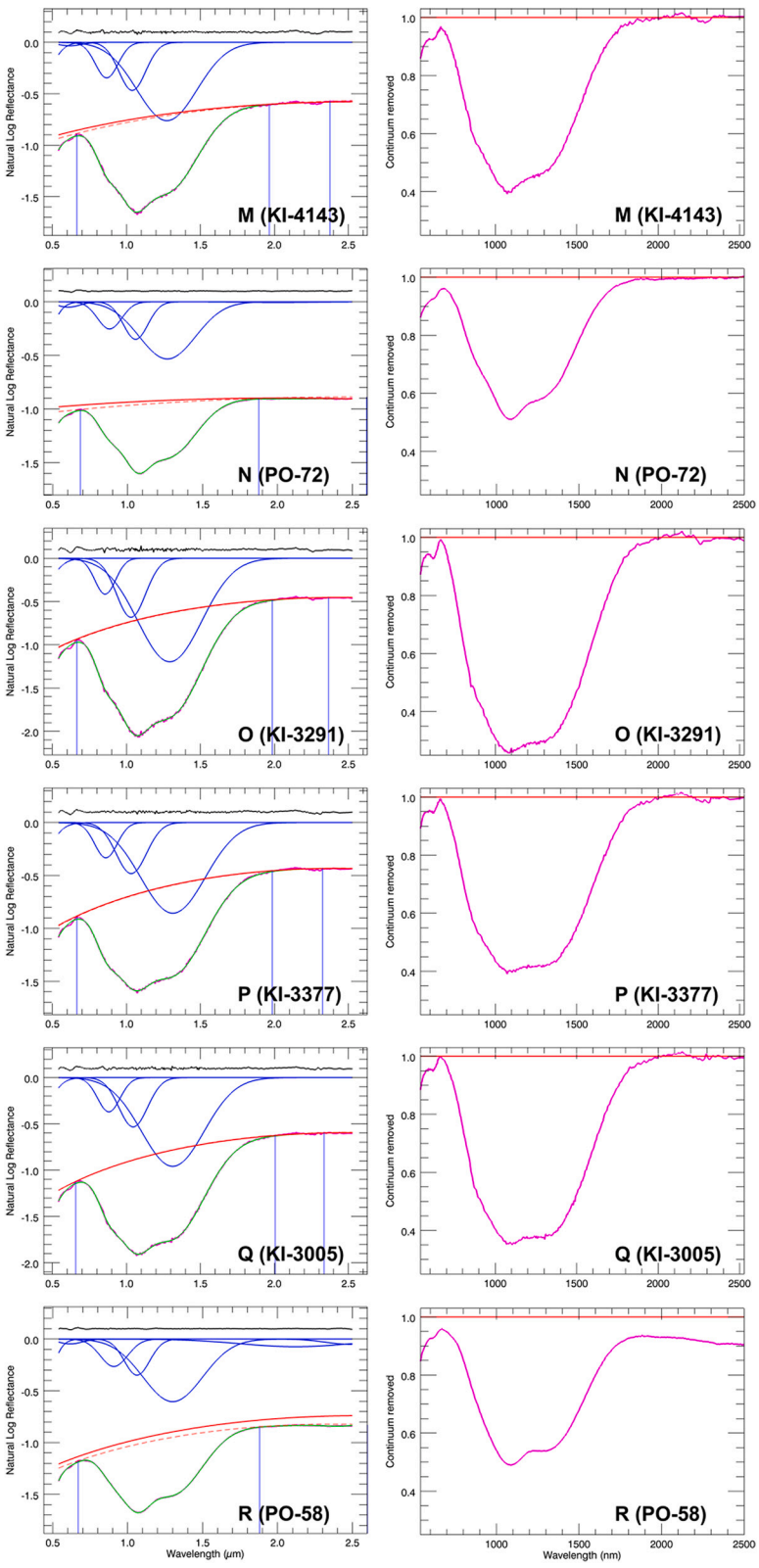

Fig. 7. (*continued*).

Table 9
MGM results for the full 'Sunshine' suite of 18 natural samples (A to R). From left to right: sample ID from RELAB spectral database, MGM used configuration (L4 (L5 without Gaussian '650 nm', L5 (see Table 1), L6 (L5 + Gaussian '2000 nm'), L7 (L5 + Gaussians '2000 nm' and '2450 nm'), Fo# actual value, Rms: integrated MGM residuals along the entire spectral domain, M1–1, M2, M1–2 band centers, band widths, band depths.

	MGM Conf.			*Band center (nm)*				*Band width (nm)*				*Band depth*			
Name		*Fo#*	*Rms*	*650*	*850*	*1050*	*1250*	*650*	*850*	*1050*	*1250*	*650*	*850*	*1050*	*1250*
A	L7	0.97	0.0023	642.2	870.6	1041.8	1223.2	200.1	190.5	168.0	401.5	−0.006	−0.072	−0.136	−0.150
B	**L7**	0.92	0.0028	637.3	852.3	1030.7	1202.4	200.2	173.5	166.3	414.2	−0.008	−0.090	−0.192	−0.246
C	L7	0.92	0.0020	633.0	866.5	1038.6	1214.9	200.4	193.0	168.6	393.8	−0.022	−0.114	−0.204	−0.241
D	**L7**	0.90	0.0020	641.6	855.6	1036.1	1205.9	199.6	194.7	167.2	400.1	−0.018	−0.126	−0.225	−0.270
E	L7	0.89	0.0022	637.2	866.3	1041.4	1219.8	197.1	208.5	168.0	418.6	−0.048	−0.174	−0.266	−0.372
F	L7	0.89	0.0050	630.0	882.6	1042.9	1223.8	195.1	202.6	170.6	412.3	−0.053	−0.195	−0.295	−0.411
G	L7	0.86	0.0038	641.9	863.5	1044.1	1219.5	199.8	237.4	175.8	420.8	−0.046	−0.188	−0.276	−0.379
H	**L7**	0.84	0.0021	626.4	858.7	1039.0	1218.6	198.9	182.6	174.9	437.3	−0.025	−0.166	−0.268	−0.383
I	**L6**	0.66	0.0067	617.6	854.8	1029.4	1242.0	86.4	193.5	203.9	443.7	−0.092	−0.439	−0.625	−0.889
J	**L4**	0.60	0.0095	–	855.3	1028.1	1252.4	–	157.9	209.1	461.9	–	−0.320	−0.532	−0.798
K	**L7**	0.51	0.0070	590.5	859.1	1035.4	1256.6	169.4	188.0	208.1	466.8	−0.080	−0.346	−0.478	−0.752
L	**L7**	0.42	0.0026	607.8	884.4	1052.2	1251.6	182.9	200.4	181.7	452.7	−0.063	−0.234	−0.302	−0.494
M	**L5**	0.41	0.0079	617.3	866.9	1039.6	1273.7	192.0	179.9	211.7	477.2	−0.034	−0.347	−0.468	−0.762
N	**L6**	0.36	0.0026	604.2	879.7	1053.5	1265.2	184.3	189.5	191.8	442.7	−0.050	−0.253	−0.350	−0.533
O	**L4**	0.29	0.0135	–	856.5	1031.1	1293.0	–	164.4	230.5	508.3	–	−0.415	−0.682	−1.197
P	**L4**	0.18	0.0090	–	861.5	1032.9	1314.3	–	178.3	240.9	512.4	–	−0.334	−0.482	−0.857
Q	**L4**	0.11	0.0092	–	881.2	1045.7	1313.1	–	177.3	226.6	497.3	–	−0.371	−0.533	−0.959
R	**L7**	0.01	0.0024	617.4	908.2	1062.5	1301.3	187.7	214.2	198.0	468.1	−0.047	−0.265	−0.349	−0.605

Table 10
Olivine composition estimates for 18 natural samples. *From left to right*: sample ID from RELAB spectral database, MGM used configuration, Fo#: actual % molar Forsterite; Fô#: predicted % molar Forsterite, "Fô#- Fo#" (predicted - actual) is a signed quantity (+ if overestimate, − if underestimate), real distances (d_{850}, d_{1050}, d_{1250}) to each M1–1, M2, M1–2 trend line, rsdt: real spectral quadratic distance to the three trends, predicted distances ($d_{850}\hat{}$, $d_{1050}\hat{}$, $d_{1250}\hat{}$) to each trend line, psdt: predicted spectral quadratic distance to the three trends. Last line 'RMS' gives the standard deviation for all quantities for the full set of 18 samples, and for the selection (in bold) of 13 samples (excluding A,C,E,F,G) (see also Table 9).

Name	*MGM Conf.*	*Fo#*	$\widehat{Fo\#}$	$\widehat{Fo\#} - Fo\#$	*real distance*				*predicted distance*			
					d_{850}	d_{1050}	d_{1250}	*rsdt*	$\widehat{d_{850}}$	$\widehat{d_{1050}}$	$\widehat{d_{1250}}$	*psdt*
A	L7	0.97	0.68	−0.290	24.41	14.38	25.57	22.03	5.35	2.98	−4.76	4.48
B	**L7**	0.92	0.91	−0.010	2.82	1.29	−0.50	1.82	2.17	0.90	−1.55	1.62
C	L7	0.92	0.76	−0.160	17.05	9.13	12.03	13.15	6.53	2.85	−4.71	4.93
D	**L7**	0.90	0.86	−0.040	4.88	5.90	0.93	4.45	2.26	4.33	−3.26	3.39
E	L7	0.89	0.72	−0.170	14.88	10.81	13.79	13.27	3.71	4.13	−3.99	3.95
F	L7	0.89	0.63	−0.260	31.17	12.29	17.75	21.89	14.09	2.08	−9.44	9.86
G	L7	0.86	0.73	−0.130	10.12	12.35	10.37	10.99	1.58	7.24	−3.22	4.66
H	**L7**	0.84	0.76	−0.080	3.97	6.39	7.39	6.09	−1.29	3.25	−0.98	2.09
I	**L6**	0.66	0.66	0.000	−11.68	−10.21	11.98	11.32	−11.68	−10.21	11.98	11.32
J	**L4**	0.60	0.59	−0.010	−15.12	−13.86	16.10	15.05	−15.77	−14.25	15.05	15.04
K	**L7**	0.51	0.53	0.020	−17.28	−10.09	10.84	13.14	−15.97	−9.30	12.93	13.02
L	**L7**	0.42	0.43	0.010	2.09	3.13	−3.60	3.00	2.75	3.52	−2.55	2.97
M	**L5**	0.41	0.39	−0.020	−16.00	−9.86	17.54	14.84	−17.32	−10.64	15.45	14.74
N	**L6**	0.36	0.36	0.000	−6.58	2.10	3.79	4.55	−6.58	2.10	3.79	4.55
O	**L4**	0.29	0.33	0.040	−34.33	−23.04	24.26	27.67	−31.70	−21.47	28.44	27.53
P	**L4**	0.18	0.17	−0.010	−36.61	−25.59	34.03	32.42	−37.27	−25.99	32.99	32.42
Q	**L4**	0.11	0.07	−0.040	−21.44	−15.56	25.54	21.24	−24.06	−17.14	21.36	21.05
R	**L7**	0.01	0.00	−0.010	−1.00	−2.67	3.21	2.48	−1.65	−3.07	2.16	2.37
RMS (all)				0.114	18.52	12.32	16.21	15.89	15.39	10.76	13.60	13.39
RMS (selection)				0.031	17.53	12.47	15.98	15.47	17.49	12.38	15.61	15.31

Isaacson et al., 2014); HA (for Han et al., 2020). It is of relevance to recall that significant differences exist in the way these solutions have been produced. As a matter of fact, SP relies on a flat continuum for the MGM modeling and was derived from spectra obtained on natural samples; IS makes use of an oblique continuum with fixed anchor points, requires MGM variable starting conditions and is focused on the [0–70] Fo# range with a limited set of synthetic samples. HA relies on a polynomial continuum and is based on a mixture of synthetic and natural samples.

In view of being able to draw some quantitative comparison, these earlier regressions Fig. 5 are implemented on the suite of 19 Suny-Bristol samples considered in the previous section of this paper and for each of them, we calculate the performances for the spectral distance to trend (rsdt, psdt) and Fô # estimates, as done with the present regression.

To better assess the differences between the different solutions, the trend lines are superposed on the same graph below (see Fig. 6).

Corresponding statistics and performances are given hereafter in Table 8 for the four regressions.

These results indicate that the PDC solution, based on the use of MGM with a degree 2 polynomial continuum, is an improvement over previous solutions. One notes, however, that SP solution is close enough in terms of predicted-actual quantities, though the distances to trend rsdt and psdt are clearly more pronounced by a factor on the order of 1.5.

3.3. Application to the natural olivine samples suite historically considered

We now consider the suite spanning the forsterite-fayalite solid solution series historically considered to derive the olivine composition

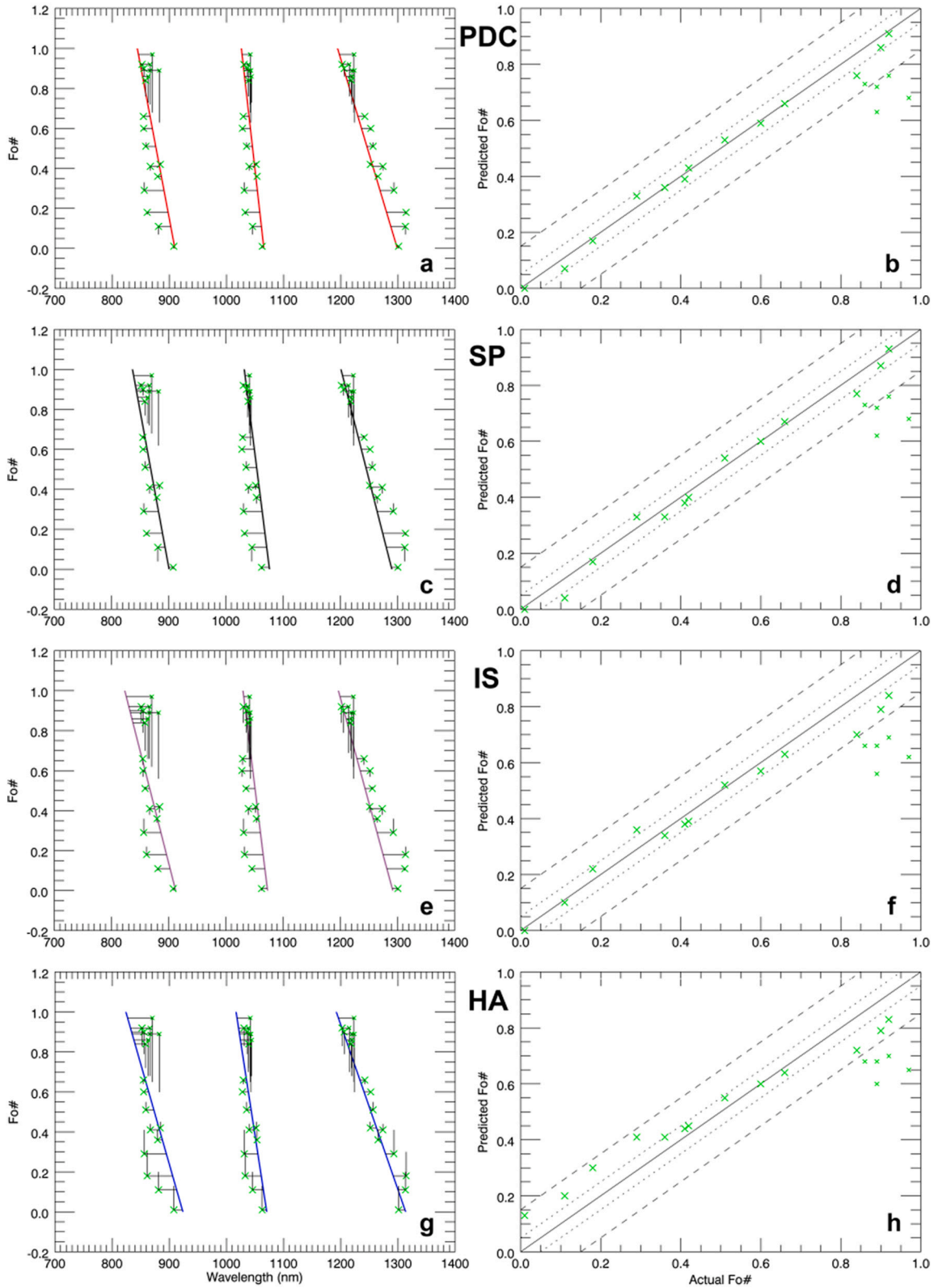

Fig. 8. *Left column:* MGM results with the 18 natural samples in Molar % Forsterite vs band center (nm) graph. Green crosses (x) plot for each sample the actual Fo# associated with M1–1, M2, M1–2 band centers determined by MGM deconvolution. The horizontal black thin bars display the real distances (d_{850}, d_{1050},d_{1250}) to trend lines for each sample while the vertical black thin bars show the "Fô#- Fo#" (i.e., predicted – actual Fo#) quantities; *Right column:* Predicted (Fô#) versus Actual (Fo#) Molar % Forsterite estimates for the 18 natural samples displayed on the left. (For interpretation of the references to colour in this figure legend, the reader is referred to the web version of this article.)

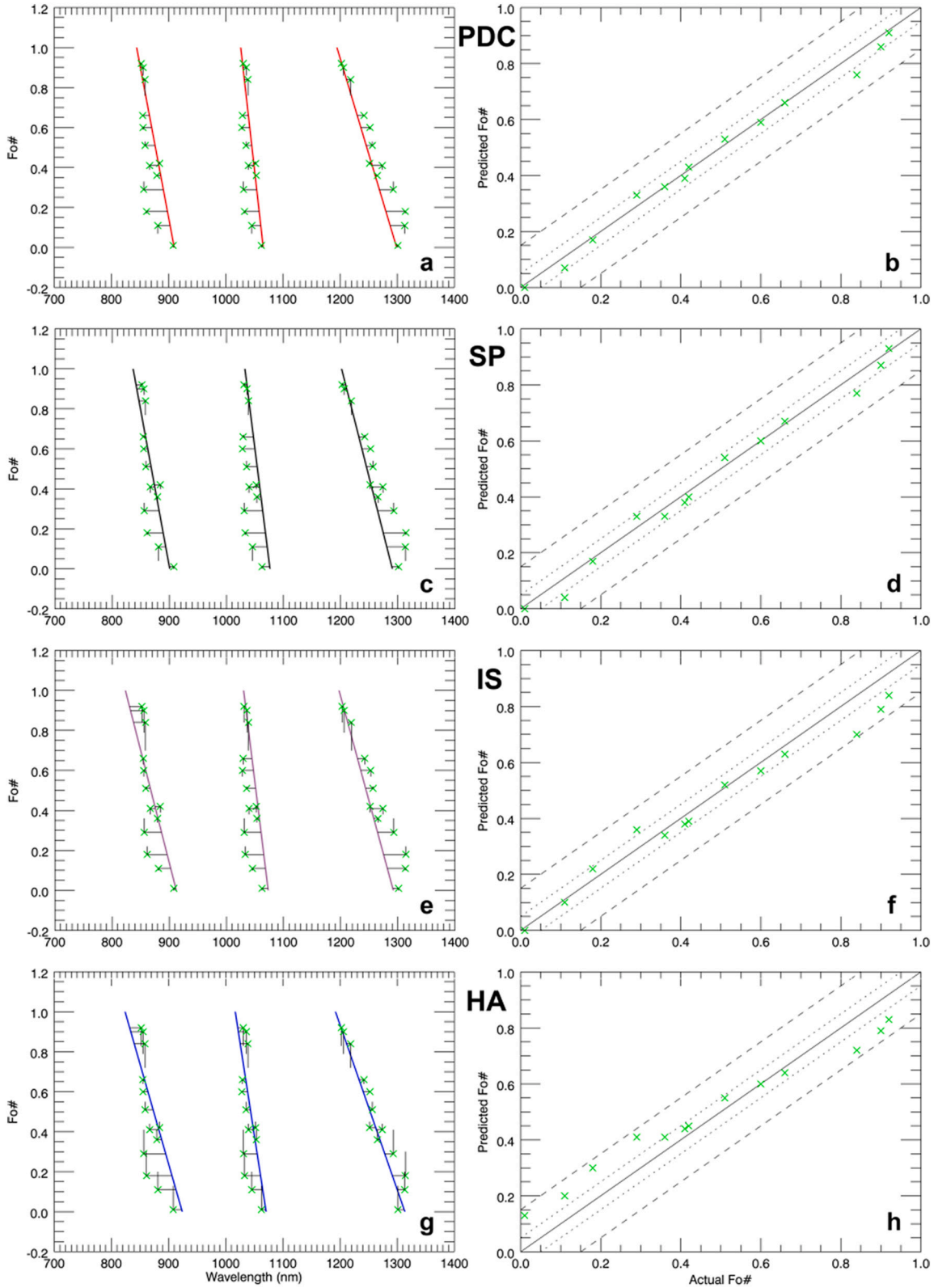

Fig. 9. *Left column:* MGM results with the 13 retained samples in Molar % Forsterite vs band center (nm) graph. Green crosses (x) plot for each sample the actual Fo# associated with M1–1, M2, M1–2 band centers determined by MGM deconvolution. The horizontal black thin bars display the real distances (d_{850}, d_{1050},d_{1250}) to trend lines for each sample while the vertical black thin bars show the "Fô#- Fo#" (i.e., predicted – actual Fo#) quantities; *Right column:* Predicted (Fô#) versus Actual (Fo#) Molar % Forsterite estimates for the 13 samples displayed on the left. (For interpretation of the references to colour in this figure legend, the reader is referred to the web version of this article.)

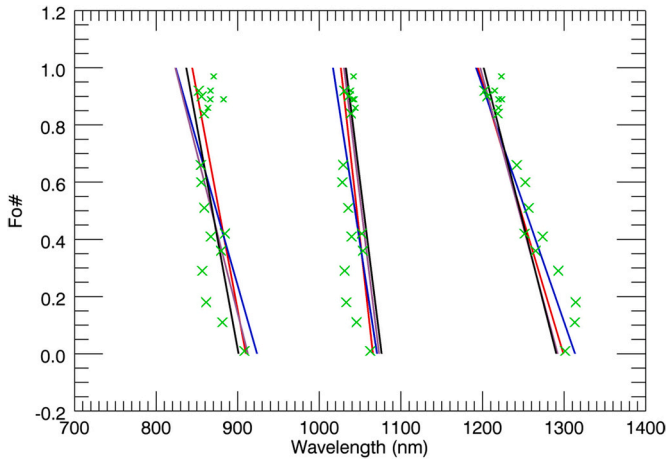

Fig. 10. Composition trend lines in Molar % Forsterite versus band center wavelength (nm) graph (in black: SP trend lines; in purple: IS trend lines from suite 1(Fo range: 0–70); in blue: HA regression (Polynomial method); in red: 'Our' current PDC trend lines. Green crosses X (large cross for each samples except for A, C, E, F, G samples (small cross)) plot for each sample the actual Fo# associated with M1–1, M2, M1–2 band centers determined by MGM deconvolution. (For interpretation of the references to colour in this figure legend, the reader is referred to the web version of this article.)

from spectral measurements (Sunshine and Pieters, 1998) and apply our MGM approach on its 18 natural samples. We note that, compared to the case of the spectra measured on synthetic samples, the MGM modeling requires more often the use of additional bands (L6, L7) to produce low integrated MGM residuals (rms) along all the continuum on the order of 0.002–0.007, which suggests that other phases are present in these natural samples (see Fig. 7 and Tables 9 and 10). The final polynomial continuum may be shifted upward with respect to the considered spectrum. Conversely, some spectra (J,O,P,Q) are modeled with four bands only (L4 configuration, i.e. L5 one without the use of Gaussian '650 nm'). For these spectra, while the overall continuum shape appears well-behaved and tangential to the spectrum all along the spectral domain, the integrated MGM residuals (rms) are more pronounced than for the other spectra, and are in the range of 0.009–0.013 (see Table 9). These observations suggest that the continuum physical understanding hides some additional complexity yet to be explored.

For all spectra, the Gaussians associated with M1–1, M2, M1–2 olivine absorption features perform quite well (see Fig. 7).

The trend line equations established from the synthetic series (see Table 5 and Fig. 3a) are then used to predict the composition variability based on the minimum deviation from the three trend lines simultaneously (see Table 10 and Figs. 8(a,b), 9(a,b)). For each sample, the best solution among L4, L5, L6 and L7 is retained and shown in Fig. 7.

While the full suite presents an integrated"Fô#-Fo#" rms deviation of 0.114, with a 15.9 nm sdt, we find that if one excludes spectra (A,C,E, F,G) (see Table 10) the suite resulting from this selection has an integrated"Fô#-Fo#" rms deviation of 0.031 (i.e., comparable to the"Fô#-Fo#" rms deviation produced with synthetic samples (see Table 7)), but with a larger rsdt of 15.5 nm (see Table 10) compared to 6 nm (see Table 7). The 5 discarded spectra correspond to Mg-rich olivines (Fo# > 86), for which our prediction underestimates Fo#. Along with Isaacson et al. (2014) and Dyar et al. (2009), we suspect these spectra are affected by impurities and/or heterogeneities arising from the presence of minor amounts of various cations (Ca^{2+}, Mn^{2+}, Ca^{2+}, Cr^{2+}, Fe^{3+}, …) which mainly disturb the position of the bandcenter for the M1–1 absorption. Indeed, the occurrence of transitional elements (e.g., Ni, Cr, Sp, Cu, Mn, S, Zn, Co…) in the crystal lattice, trapped in minerals even at trace levels may significantly influence the splitting through a change of distances between ions (Shkuratov et al., 2011) which may reflect in the absorption feature.

One notes that the band widths of the three gaussians 850, 1050, 1250 nm are well grouped with the following respective means and standard deviations: 190 ±18 nm, 192±24 nm, 446±36 nm for the full suite, and: 184 ±14 nm, 201±23 nm, 460±32 nm for the subsuite after selection.

Table 11
Statistical performances for the 4 compared solutions, with rms standard deviation for all quantities, implemented on the full suite of 18 natural olivine samples used by Sunshine and Pieters (1998), and on a selection of 13 samples, excluding Mg-rich samples with Fo# > 86.

	RMS (considered regression)	$\widehat{Fo\#} - Fo\#$	*real distance (nm)*				*predicted distance (nm)*			
			d_{850}	d_{1050}	d_{1250}	***rsdt***	$\widehat{d_{850}}$	$\widehat{d_{1050}}$	$\widehat{d_{1250}}$	***psdt***
all	*RMS (PDC)*	**0.114**	18.52	12.32	16.21	**15.89**	15.39	10.76	13.60	**13.39**
	RMS (SP)	**0.116**	18.69	16.55	17.01	**17.44**	13.58	16.67	16.03	**15.48**
	RMS (IS)	**0.154**	25.68	14.94	17.85	**20.01**	14.70	14.45	18.08	**15.83**
	RMS (HA)	**0.150**	27.34	15.89	13.16	**19.77**	14.46	9.57	15.81	**13.55**
selection	*RMS (PDC)*	**0.031**	17.53	12.47	15.98	**15.47**	17.49	12.38	15.61	**15.31**
	RMS (SP)	**0.035**	13.53	19.17	18.71	**17.33**	13.21	19.44	18.19	**17.16**
	RMS (IS)	**0.061**	18.18	16.91	18.80	**17.98**	14.71	16.78	20.06	**17.32**
	RMS (HA)	**0.084**	22.35	13.99	10.92	**16.48**	15.10	10.39	16.73	**14.33**

Table 12
Olivine composition estimates for 4 natural (2 terrestrial, 2 lunar) samples. *From left to right*: sample ID from RELAB spectral database, MGM used configuration, MGM Rms: integrated MGM residuals along the entire spectral domain, Fo#: actual % molar Forsterite; Fô#: predicted % molar Forsterite, "Fô#- Fo#" (predicted-actual) is a signed quantity (+ if overestimate, − if underestimate), real distances (d_{850}, d_{1050},d_{1250}) to each M1-1, M2, M1-2 trend line, rsdt: real spectral quadratic distance to the three trends, predicted distances ($d_{850}\hat{}$, $d_{1050}\hat{}$, $d_{1250}\hat{}$) to each trend line, psdt: predicted spectral quadratic distance to the three trends. For LR-CMP-227 sample, 3 solutions are compared (see Figs. 12 and 14) as discussed in the text. MGM retained configurations are shown in bold.

Name	*MGM Conf.*	*MGM Rms*	*Fo#*	$\widehat{Fo\#}$	$\widehat{Fo\#} - Fo\#$	*real distance*				*predicted distance*			
						d_{850}	d_{1050}	d_{1250}	*rsdt*	$\widehat{d_{850}}$	$\widehat{d_{1050}}$	$\widehat{d_{1250}}$	*psdt*
GDS-71b	**L7**	0.0048	0.91	0.88	−0.030	4.30	−2.89	2.72	3.38	2.33	−4.07	−0.41	2.72
AG-TJM-08	**L5**	0.0027	0.90	0.91	0.010	−9.59	−0.73	5.42	6.37	−8.94	−0.34	6.46	6.37
LR-CMP-227	L4	0.0124	0.87	0.66	−0.210	−6.84	−6.93	40.83	24.23	−20.65	−15.18	18.87	18.37
LR-CMP-227	L5	0.0040	0.87	0.82	−0.050	−3.24	−7.38	13.57	9.11	−6.52	−9.35	8.34	8.15
LR-CMP-227	**L7**	0.0023	0.87	0.85	−0.020	−3.81	−5.73	7.42	5.84	−5.13	−6.52	5.33	5.69
LR-CMP-169	**L6**	0.0073	0.48	0.53	0.050	−18.85	−18.88	11.06	16.67	−15.56	−16.91	16.29	16.26

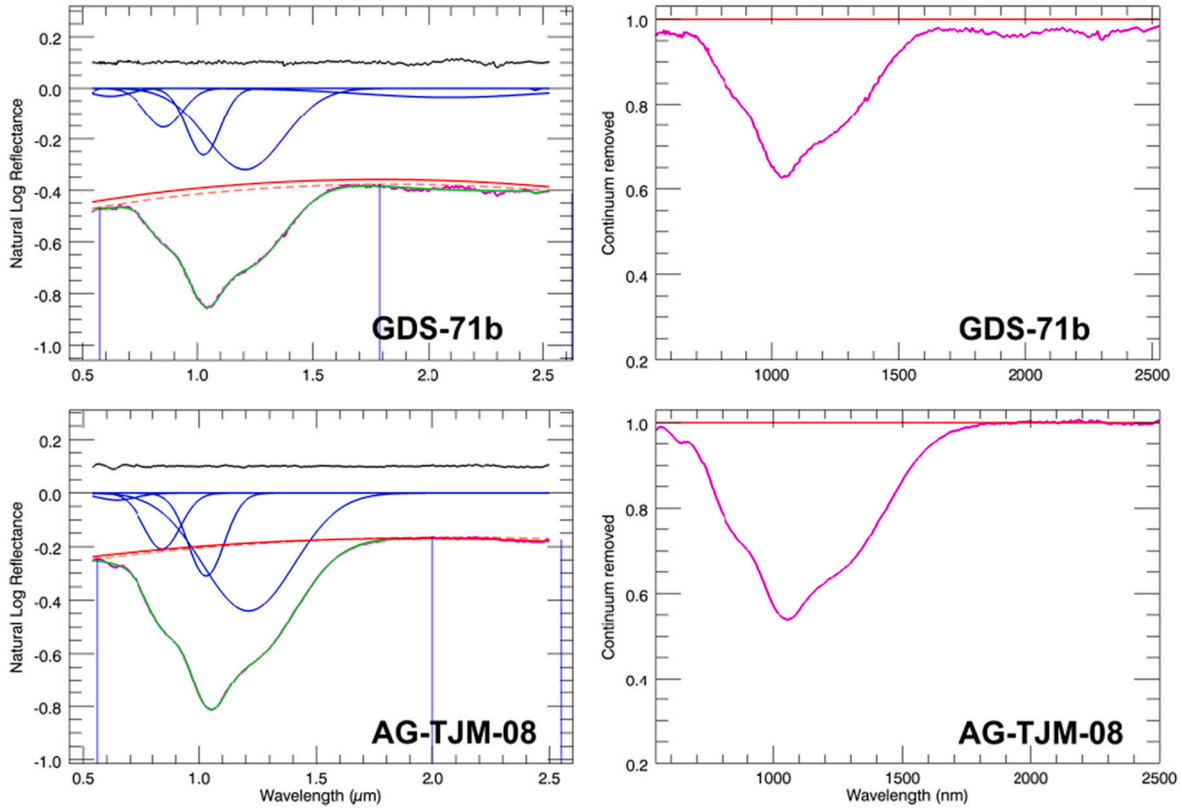

Fig. 11. *Left.* MGM deconvolution on spectra of terrestrial samples (GDS-71b, AG-TJM-08) with high Fo#. Measured spectrum (pink line) and MGM modeled one (green solid line) with the Gaussians (solid blue lines) and polynomial (dashed -starting continuum- and solid -final continuum after running MGM- red lines) and the residuals line in black along the spectral domain. For clarity, the residuals (observed - modeled quantity) are shifted by +0.1 which means that a perfect fit is displayed with a 0.1 flat line. Position of the local maxima (anchor points) along the spectrum used for the process of initialization shown by thin vertical blue lines (3rd anchor point not displayed if beyond 2.5 μm). *Right.* Corresponding spectra shown in pink after polynomial final continuum removal (red line). (For interpretation of the references to colour in this figure legend, the reader is referred to the web version of this article.)

The main difference compared to the results obtained on the same series by (Sunshine and Pieters, 1998) is that the average width of the band describing the M1–1 absorption is decreased from 245 nm to 190 nm, while the width for M2 absorption is very slightly increased, and unmodified for the M1–2 absorption band, in agreement with the results found with the synthetic Suny-Bristol samples. This is a consequence of the curvature of the polynomial continuum compared to the flat one previously considered. It may also be related to the introduction of the 650 nm band in the modeling.

While our results in terms of Fo# prediction appear more satisfactory than with previous derivations (see Figs. 8, 9, 10 and Table 11), we also do find that O, P, Q spectra are shifted and slightly off trend lines as noted in previous studies and we cannot come up with an explanation for this.

The statistical performances for each solution applied to the set of natural samples (Table 11) reflect the same relative ranking as noted previously (Table 8) in the case of synthetic samples, but with an overall greater distance to the trend lines. The removal of the Mg-rich olivines (Fo# > 86) (Fig. 9) for which our prediction underestimates Fo# has a dramatic effect on the "Fô#- Fo#" (i.e., predicted – actual Fo#) rms deviation, but do not significantly modify the statistics in terms of distances to trends, which remain large for natural samples compared to the synthetic ones.

3.4. Application to other natural terrestrial and lunar samples

The purpose of this section is to highlight several advantages / capabilities of the currently proposed 'PDC' solution.

First of all, at variance with the 5 spectra discarded in the previous section (see Table 11 and Figs. 8, 9), our approach is able to provide with reliable Fo# estimates when considering high Fo# natural terrestrial samples. Two examples are given below (see Table 12) with GDS-71b (grain size <60 μm) (King and Ridley, 1987) and AG-TJM-08 (grain size <45 μm) samples, respectively taken from the USGS (Kokaly et al., 2017; https://speclab.cr.usgs.gov/spectral-lib.html) and RELAB (http://www.planetary.brown.edu/relab/) collections. As shown on Fig. 11, the results from the MGM modeling reveal that while for AG-TJM-08 the L5 configuration is performing very well, L7 is to be used for GDS-71b, with the continuum being slightly shifted upward all along the spectrum. For both cases, the spectral quadratic distances rsdt and psdt to the three trends are quite low with Fo# predictions close to the actual molar forsterite number (see Table 12).

Then, this approach is also implemented on two lunar samples (LR-CMP-227 and LR-CMP-169) (grain size <125 μm) (http://www.planetary.brown.edu/relab/). The example with LR-CMP-227 (olivine sample from troctolite separate76535,94 (Gooley et al., 1974)) is very much telling (see Table 12): it shows that the non consideration of the long-ward absorptions beyond 1.6 μm has a significant impact both on the

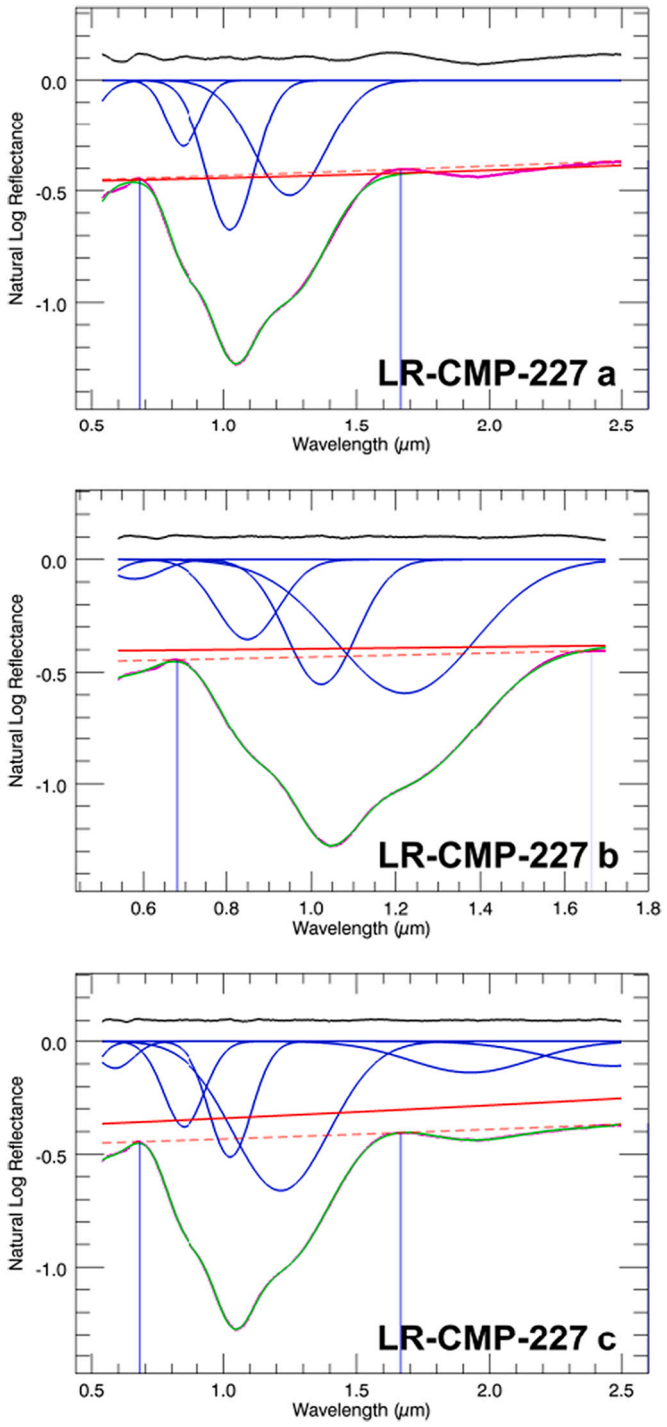

Fig. 12. MGM modeling of LR-CMP-227 lunar spectrum (troctolite sample76535 (Gooley et al., 1974)) with 3 different configurations. **(a).** L4 configuration applied over the full spectral domain leading to a non physical solution with the depth of M2 absorption feature deeper than M1–2 one; **(b).** L5 configuration applied with a spectral cutoff at 1700 nm; **(c).** L7 configuration applied over the full spectral domain.

deconvolution process and subsequent Fo# estimate derivation and can be quite critical, especially for lunar olivines which usually contain small, but spectrally significant abundances of tiny inclusions of dark Cr-spinels (e.g., Papike et al., 1998) that have strong absorption beyond 1.6 μm (Cloutis et al., 2004; Isaacson and Pieters, 2010; Isaacson et al., 2011a, 2011b) or for some olivine diogenites (e.g., NWA 6232) (Carli et al., 2018). While the solution with L5 configuration, with a spectral cutoff at 1700 nm as proposed by Isaacson and Pieters (2010) represents a clear improvement over the L4 configuration (see Fig. 12), the L7 solution implemented over the full spectral domain appears even better for Fo# determination, with quite low MGM rms residuals, rsdt and psdt. As seen previously, we note that the continuum is shifted upward, thus no longer tangent to the overall spectrum. Another example of MGM deconvolution performed on LR-CMP-169 spectrum, measured on the lunar sample low-Ti basalt15555 with Fe-rich composition, is given on Fig. 13. The L6 configuration used handles pretty well the pronounced long-wavelength spinel absorption likely due to chromite-bearing inclusions (Cheek and Pieters, 2014). As noted in other previous cases, the continuum is shifted upward. The M1–1, M2 and M1–2 olivine absorptions are well-behaved, with a predicted Fo# estimate of 53, which could reflect a correct value, as olivine in thin section of 15,555 ranges from Fo# 10 to 65, with most analyses yielding Fo# ~55 (Isaacson et al., 2011b; Kremer et al., 2020). The MGM rms residuals and the rather large rsdt, psdt quantities suggest that the modeling, though acceptable as is, could still be improved.

The two lunar cases discussed above demonstrate that both, the general methodology based on a full wavelength deconvolution along the visible and near-infrared range (540–2600 nm), and the trend lines derived from the current PDC solution perform well, even when considering the complex situation of chromite-bearing lunar olivines (e.g., Isaacson and Pieters, 2010; Shkuratov et al., 2011; Pinet et al., 2020…).

The table of goodness of fit below (Table 13) shows that PDC is doing slightly better than SP, with both regressions giving close results when considering rather high Fo#. The main difference between PDC and SP is for the spectral distance to trend estimates (rsdt, psdt) which are systematically larger for SP compared to PDC (see also Table 8 for synthetic samples and Table 11 for natural samples). This result points toward the fact that band centers are better determined with the proposed current MGM implementation.

4. Implications and conclusions

The current MGM modeling, with the handling of the overall continuum by a second-order polynomial initially adjusted on the main maxima along the reflectance spectrum, is a clear progress. This approach is close to the convex hull one, but is more flexible in the sense that it does not constrain the continuum to be tangential to the spectrum though it does not preclude it. Continuum slopes are well known to be highly variable, being affected by a number of parameters, which include surface texture, grain size, viewing geometry, and alteration due to space weathering. The results which are produced here, all particularly with natural samples, suggest that the continuum physical understanding hides additional complexity yet to be explored. The robustness of the proposed solution is also significantly increased by the use of a fixed set of starting conditions able to address situations ranging from laboratory to orbital data.

The band center positions of the three primary olivine absorptions (M1–1, M2, M1–2) are used simultaneously to produce a constrained prediction across an extended range Fo#[0–90] of olivine solid solution composition. The established trend lines based on synthetic samples with composition ranging from Fo#0 to #90 appear robust when implemented on natural samples (including lunar samples), and represent an improvement over previous solutions.

Both, the general methodology based on a full wavelength deconvolution along the visible and near-infrared range (540-2600 nm), and the trend lines Fo#/100 = a*λ(nm) + b derived from the current solution (Table 14) (referred to as PDC) perform well, even when considering the complex situation of chromite-bearing lunar olivines. Furthermore, the procedure developed and proposed here, through its separate and quadratic estimates to the trends, offers an assessment to qualify the Fo# determination made on unknown samples and/or remote sensing observations.

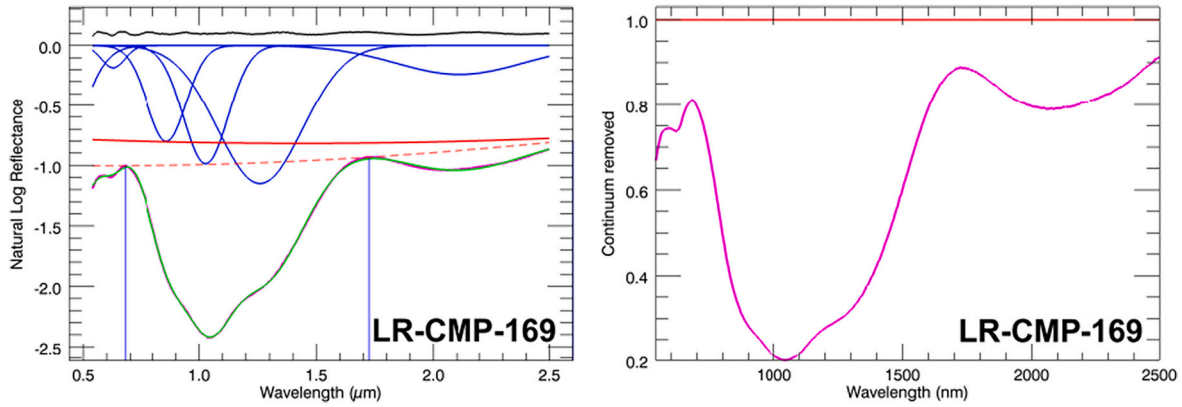

Fig. 13. *Left.* MGM deconvolution on lunar spectrum LR-CMP-169 (sample 15,555) with rather low Fo# indicative of Fe-rich composition. Measured spectrum (pink line) and MGM modeled one (green solid line) with the Gaussians (solid blue lines) and polynomial (dashed-(starting continuum- and solid -final continuum after running MGM- red lines) and the residuals line in black along the spectral domain. For clarity, the residuals (observed – modeled quantity) are shifted by +0.1 which means that a perfect fit is displayed with a 0.1 flat line. Position of the local maxima (anchor points) along the spectrum used for the process of initialization shown by thin vertical blue lines (3rd anchor point not displayed if beyond 2.5 μm). *Right.* Corresponding spectrum shown in pink after polynomial final continuum removal (red line). (For interpretation of the references to colour in this figure legend, the reader is referred to the web version of this article.)

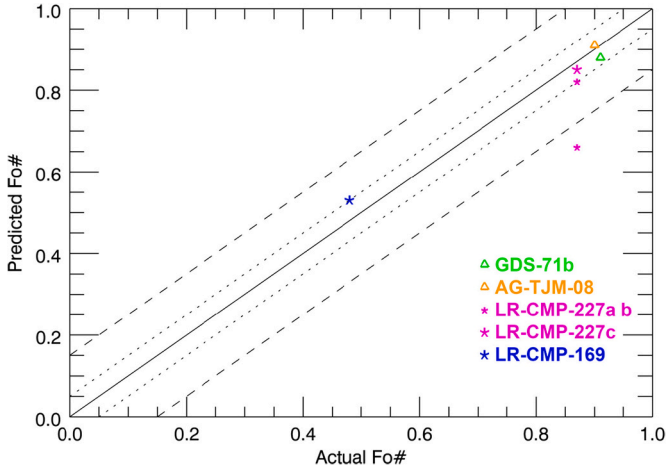

Fig. 14. Predicted (Fô#) versus Actual (Fo#) Molar % Forsterite estimates for 4 natural (2 terrestrial, 2 lunar) samples (see Table 12). Triangles correspond to terrestrial high-Mg olivine spectra (green for GDS-71b and brown for AG-TJM-08) while stars correspond to lunar olivine spectra (Pink for LR-CMP-227a (small star), LR-CMP-227b (small star),LR-CMP-227c (large star); blue star for LR-CMP-169). (For interpretation of the references to colour in this figure legend, the reader is referred to the web version of this article.)

Natural samples can indeed be found with variable grain sizes or as rock slabs/chips and are likely not devoid of minor amount of cations such as Fe3+, Cr2+, Mn2+, Ca2+, … which may disturb the optical properties across the olivine composition range. The current approach based on synthetic samples provides a reference frame which is as free as possible of distortion effects.

As an operational guideline, the deconvolution based on L5 configuration should be used first (with L4, L6, L7 as alternatives), and the results should be assessed on the basis of the MGM rms residuals, the spectral distances to trend quantities rsdt and psdt. The lower these quantities, the more reliable the Fo# estimate, on the order of 3–5 Fo# or better when rsdt <5–7 nm. Conversely, if the spectral distance to trend quantities are high, more caution should be put on the interpretation. If rsdt and psdt quantities remain high, while MGM modeling outcomes are fine, H2O contamination, impurities and/or other mineral phases, or grain size and texture related issues (e.g., Carli and Sgavetti, 2011; Carli et al., 2015; Serventi and Carli, 2017) are likely to be involved in the sample (or pixel) under consideration. These spectral distance to trend quantities (rsdt, psdt) should be systematically considered as a diagnostic tool in planetary exploration when processing and dealing with the interpretation of remote sensing datasets in terms of olivine composition.

With the ongoing development of a multi-technique payload strategy, particularly in the context of in situ planetary exploration, the same sample can now be remotely documented through an integrated approach frequently combining microscopic imaging, elemental geochemistry and optical spectroscopy (e.g., Ehlmann et al., 2017; Wiens et al., 2021; Maurice et al., 2021). This gives access to a more comprehensive description of the samples, typically involving their surface state and texture (e.g., rock or soil (grain size, cristallinity, …)), elemental composition, and spectral characteristics (absorption

Table 14
Linear regression equations Fo# /100 = a*λ(nm) + b for the three diagnostic M1–1 ('850'), M2 ('1050'), M1–2 ('1250') trend lines.

850		*1050*		*1250*	
a	*b*	*a*	*b*	*a*	*b*
−0.015216	13.845	−0.025450	27.119	−0.0095610	12.421

Table 13
4 natural (2 terrestrial (GDS-71b, AG-TJM-08), 2 lunar (LR-CMP-227; LR-CMP-169)) samples with the MGM retained solutions shown in bold in Table 12. Statistical performances for the 4 compared solutions, with rms standard deviation for all quantities.

RMS (considered regression)	$\widehat{Fo\#} - Fo\#$	*real distance (nm)*				*predicted distance (nm)*			
		d_{850}	d_{1050}	d_{1250}	***rsdt***	$\widehat{d_{850}}$	$\widehat{d_{1050}}$	$\widehat{d_{1250}}$	***psdt***
RMS (PDC)	**0.031**	10.96	9.98	7.32	**9.54**	9.40	9.29	9.16	**9.29**
RMS (SP)	**0.034**	8.22	16.22	6.37	**11.12**	6.87	14.95	9.20	**10.88**
RMS (IS)	**0.069**	15.04	14.06	7.62	**12.68**	8.96	14.87	9.63	**11.46**
RMS (HA)	**0.081**	15.14	9.65	5.70	**10.88**	7.65	6.94	8.02	**7.55**

features, continuum, …). In this context and even more so in the future, the method proposed here should take advantage of all the available information and aid in the analyses of olivine-dominated spectra.

Declaration of Competing Interest

None.

Acknowledgements

This work was supported by the French Space Agency (CNES) in projects in conjunction with the Mars-Express mission / OMEGA instrument and chang'e-4 mission /VNIS instrument. We also acknowledge the thorough and constructive reviews from C. Carli and an anonymous reviewer which greatly improved the quality and clarity of the manuscript.

References

Brown, A.J., Viviano, C.E., Goudge, T.A., 2020. Olivine-carbonate mineralogy of the Jezero Crater Region. J. Geophys. Res. Planets 125, e2019JE006011. https://doi.org/10.1029/2019JE006011.

Burns, R.G., 1970. Crystal field spectra and evidence of cation ordering in olivine minerals. Am. Mineral. 55, 1608–1632.

Burns, R.G., 1993. Mineralogical Applications of Crystal Field Theory, second ed. Cambridge Univ. Press, Cambridge, UK, p. 551.

Carli, C., Sgavetti, M., 2011. Spectral characteristics of rocks: effects of composition and texture and implications for the interpretation of planet surface compositions. Icarus Vol. 211 (Issue: 2), 1034–1048.

Carli, C., Serventi, G., Sgavetti, M., 2015. VNIR spectral characteristics of terrestrial igneous effusive rocks: mineralogical composition and the influence of texture. In: Volcanism and Tectonism across the Inner Solar System Book Series, Vol. 401. Geological Society, Special Publication, pp. 139–158.

Carli, C., Pratesi, G., Moggi-Cecchi, V., Zambon, F., Capaccioni, F., Santoro, S., 2018. Northwest Africa 6232: visible–near infrared reflectance spectra variability of an olivine diogenite. Meteorit. Planet. Sci. 53 (Nr 10), 2228–2242. https://doi.org/10.1111/maps.13056.

Cheek, L.C., Pieters, C.M., 2014. Reflectance spectroscopy of plagioclase-dominated mineral mixtures: implications for characterizing lunar anorthosites remotely. Am. Mineral. Vol. 99, 1871–1892.

Clark, R.N., Roush, T.L., 1984. Reflectance spectroscopy: quantitative analysis techniques for remote sensing applications. J. Geophys. Res. 89 (B7), 6329–6340.

Clenet, H., Pinet, P., Daydou, Y., Heuripeau, F., Rosemberg, C., Baratoux, D., Chevrel, S. D., 2011. A new systematic approach using the modified Gaussian model: insight for the characterization of olivine-pyroxene mixtures and minerals chemicals compositions. Icarus 213, 404–422.

Clenet, H., Pinet, P.C., Ceuleneer, G., Daydou, Y., Heuripeau, F., Rosemberg, C., Bibring, J.-P., Bellucci, G., Altieri, F., Gondet, B., 2013. A systematic mapping procedure based on the modified gaussian model to characterize magmatic units from olivine/pyroxenes mixtures: application to the syrtis major volcanic shield on mars. J. Geophys. Res. Planets 118, 2013. https://doi.org/10.1002/Jgre.20112.

Cloutis, E.A., Sunshine, J.M., Morris, R.V., 2004. Spectral reflectance compositional properties of spinels and chromites: implications for planetary remote sensing and geothermometry. Meteorit. Planet. Sci. 39, 545–565. https://doi.org/10.1111/j.1945-5100.2004.tb00918.x.

Crown, D.A., Pieters, C.M., 1987. Spectral properties of plagioclase and pyroxene mixtures and the interpretation of lunar soil spectra. Icarus 72, 492–506.

Dyar, M.D., et al., 2009. Spectroscopic characteristics of synthetic olivine: an integrated multi-wavelength and multi-technique approach. Am. Mineral. 94 (7), 883–898. https://doi.org/10.2138/am.2009.3115.

Ehlmann, B.L., Edgett, K.S., Sutter, B., Achilles, C.N., Litvak, M.L., Lapotre, M.G.A., Fraeman, A.A., Arvidson, R.E., Blake, D.F., Bridges, N.T., Conrad, P.G., Cousin, A., Downs, R.T., Gabriel, T.S.J., Gellert, R., Hamilton, V.E., Hardgrove, C., Johnson, J. R., Kuhn, S., Mahaffy, P.R., Maurice, S., Mchenry, M., Meslin, P.-Y., Ming, D.W., Minitti, M.E., Morookian, J.M., Morris, R.V., Connell-Cooper, C.D.O., Pinet, P.C., Rowland, S.K., Schröder, S., Siebach, K.L., Stein, N.T., Sullivan, R., Thompson, L.M., Vaniman, D.T., Vasavada, A.R., Wellington, D.F., Wiens, R.C., Yen, A.S., 2017. Chemistry, mineralogy, and grain properties at namib and high dunes, bagnold dune field, gale crater, mars: a synthesis of curiosity rover observations. JGR-Planets 122 (12), 2510–2543.

Gooley, R., Brett, B., Warner, J., Smyth, J.R., 1974. A lunar rock of deep origin; sample 76535. Geochim. Cosmochim. Acta 38, 1329–1339.

Hamilton, V.E., 2010. Thermal infrared (vibrational) spectroscopy of Mg–Fe olivines: a review and applications to determining the composition of planetary surfaces. Chem. Erde 70, 7–33. https://doi.org/10.1016/j.chemer.2009.12.005.

Hamilton, V.E., Christensen, P.R., 2005. Evidence for extensive, olivine-rich bedrock on Mars. Geology 33 (6), 433–436. https://doi.org/10.1130/G21258.1.

Han, H.-J.X.-P. Lu, Yang, Y.-Z., Zhang, H., Mutelo, A.M., 2020. Study of the modified Gaussian model on olivine diagnostic spectral feature and its applications in space weathering experiments. Res. Astron. Astrophys. 20 (8), 129. https://doi.org/10.1088/1674–4527/20/8/129.

Isaacson, P.J., Pieters, C.M., 2010. Deconvolution of lunar olivine reflectance spectra: implications for remote compositional assessment. Icarus 210 (1), 8–13.

Isaacson, P.J., Pieters, C.M., Besse, S., Clark, R.N., Head, J.W., Klima, R.L., Mustard, J.F., Petro, N.E., Staid, M.I., Sunshine, J.M., Taylor, L.A., Thaisen, K.G., Tompkins, S., 2011a. Remote compositional analysis of lunar olivine-rich lithologies with Moon Mineralogy Mapper (M3) spectra. J. Geophys. Res. 116, E00G11.

Isaacson, P.J., Basu Sarbadhikari, A., Pieters, C.M., Klima, R.L., Hiroi, T., Liu, Y., Taylor, L.A., 2011b. The lunar rock and mineral characterization consortium: deconstruction and integrated mineralogical, petrologic, and spectroscopic analyses of mare basalts. Meteorit. Planet. Sci. 46, 228–251. https://doi.org/10.1111/j.1945-5100.2010.01148.x.

Isaacson, P.J., Klima, R.L., Sunshine, J.M., Cheek, L.C., Pieters, C.M., Hiroi, T., et al., 2014. Visible to near-infrared optical properties of pure synthetic olivine across the olivine solid solution. Am. Mineral. 99 (2–3), 467–478. https://doi.org/10.2138/am.2014.4580.

Kanner, L.C., Mustard, J.F., Gendrin, A., 2007. Assessing the limits of the modified Gaussian model for remote spectroscopic studies of pyroxenes on Mars. Icarus 187, 442–456.

King, T.V., Ridley, W.I., 1987. Relation of the spectroscopic reflectance of olivine to mineral chemistry and some remote sensing implications. J. Geophys. Res. 92, 11,457–11,469. https://doi.org/10.1029/JB092iB11p11457.

Klima, R.L., Pieters, C.M., Dyar, M., 2007. Spectroscopy of synthetic Mg–Fe pyroxenes I: spin-allowed and spin-forbidden crystal field bands in the visible and near infrared. Meteorit. Planet. Sci. 42, 235–253.

Koeppen, W.C., Hamilton, V.E., 2008. Global distribution, composition, and abundance of olivine on the surface of Mars from thermal infrared data. J. Geophys. Res. 113, E05001 https://doi.org/10.1029/2007JE002984.

Kokaly, R.F., Clark, R.N., Swayze, G.A., Livo, K.E., Hoefen, T.M., Pearson, N.C., Wise, R. A., Benzel, W.M., Lowers, H.A., Driscoll, R.L., Klein, A.J., 2017. USGS Spectral Library Version 7: U.S. Geological Survey Data Series, 1035, p. 61. https://doi.org/10.3133/ds1035.

Kremer, C.H., Mustard, J.F., Pieters, C.M., 2020. Cross-over infrared spectroscopy: a new tool for the remote determination of olivine composition. Geophys. Res. Lett. 47 (e2020GL089151) https://doi.org/10.1029/2020GL089151.

Lane, M.D., Glotch, T.D., Dyar, M.D., Pieters, C.M., Klima, R.L., Hiroi, T., 2011. Midinfrared spectroscopy of synthetic olivines: thermal emission, specular and diffuse reflectance, and attenuated total reflectance studies of forsterite to fayalite. J. Geophys. Res. 116, E08010.

Li, C., Liu, D., Liu, B., Ren, X., Liu, J., He, Z., Zuo, W., Zeng, X., Xu, R., Tan, X., Zhang, X., Chen, W., Chen, W., Shu, R., Zhang, H., Ouyang, Z., 2019. Chang'E-4 initial spectroscopic identification of lunar far-side mantle-derived materials. Nature 569, 378–382.

Lucey, P.G., 1998. Model near-infrared optical constants of olivine and pyroxene as a function of iron content. J. Geophys. Res. 103, 1703–1713.

Maurice, S., et al., 2021. The SuperCam instrument suite on the Mars 2020 rover: science objectives and mast-unit description. Space Sci. Rev. (SSR) 217 (Issue: 3). https://doi.org/10.1007/s11214-021-00807-w. Article Number: 47.

Mustard, J.F., Hays, J.E., 1997. Effects of hyperfine particles on reflectance spectra from 0.3 to 2.5 lm. Icarus 125, 145–163.

Noble, S.K., Pieters, C.M., Hiroi, T., Taylor, L.A., 2006. Using the modified Gaussian model to extract quantitative data from lunar soils. J. Geophys. Res. 111, E11009 https://doi.org/10.1029/2006JE002721.

Ody, A., Poulet, F., Bibring, J.P., Loizeau, D., Carter, J., Gondet, B., Langevin, Y., 2013. Global investigation of olivine on Mars: insights into crust and mantle compositions. J. Geophys. Res. Planets 118, 234–262. https://doi.org/10.1029/2012JE004149.

Papike, J.J., Ryder, G., Shearer, C.K., 1998. Lunar samples. In: Papike, J.J. (Ed.), Planetary Materials. Mineral. Soc. of Am, Washington, D. C, pp. 5-1–5-234.

Parente, M., Makarewicz, H.D., Bishop, J.L., 2011. Decomposition of mineral absorption bands using nonlinear least squares curve fitting: application to Martian meteorites and CRISM data. Planet, Space Sci. 59, 423–442.

Pinet, P.C., Glenadel-Justaut, D., Daydou, Y., Ceuleneer, G., Gou, S., Launeau, P., Chevrel, S., Carli, C., August 2016. MGM Deconvolution of Complex Mafic Mineralogy Rock Slab Spectra from Visible-Near Infrared Imaging Spectroscopy : Implications for the Characterization of the Terrestrial Oceanic and Lunar Crust, 4 pp., #68, Proceedings Whispers 8th Conference, L.A., California.

Pinet, P.C., Chevrel, S.D., Daydou, Y.H., 2018. Characterization of the Olivine/Plagioclase Mineralogy at Copernicus Crater from MGM Deconvolution of M3 Observations, LPSC 49th, #1899, Houston, TX.

Pinet, P.C., Chevrel, S.D., Daydou, Y.H., 2019. Reassessing the Relationship between Olivine Composition and Reflectance Spectroscopy from Advanced MGM Deconvolution, LPSC 50th, #1806, Houston, TX.

Pinet, P.C., Chevrel, S.D., Daydou, Y.H., Dhingra, D., 2020. Olivine Detection and Composition Determination at Copernicus and Eratosthenes Craters, ELS 8th proceedings, pp. 102–103 held 12–14 May(oral online). https://els2020.arc.nasa.gov/playback.

Pompilio, L., Pedrazzi, G., Sgavetti, M., Cloutis, E.A., Craig, M.A., Roush, T.L., 2009. Exponential Gaussian approach for spectral modeling: the EGO algorithm I.Band saturation. Icarus 201, 781–794.

Poulet, F., Gomez, C., Bibring, J.-P., Langevin, Y., Gondet, B., Pinet, P., Bellucci, G., Mustard, J.F., 2007. Martian surface mineralogy from Observatoire pour la Minéralogie, l'Eau, les Glaces et l'Activité on board the Mars Express spacecraft (OMEGA/MEx): Global mineral maps. J. Geophys. Res. 112, B08802 https://doi.org/10.1029/2006JE002840.

Poulet, F., Bibring, J.-P., Langevin, Y., Mustard, J.F., Mangold, N., Vincendon, M., Gondet, B., Pinet, P., Bardintzeff, J.-M., Platevoet, B., 2009. Quantitative compositional analysis of martian mafic regions using the MEx/OMEGA reflectance data. 1. Methodology, uncertainties and examples of application. Icarus 201 (1), 69–83.

Serventi, G., Carli, C., 2017. The role of very fine particle sizes in the reflectance spectroscopy of plagioclase-bearing mixtures: new understanding for the interpretation of the finest sizes of the lunar regolith. Icarus 293, 157–171. https://doi.org/10.1016/j.icarus.2017.04.018.

Serventi, G., Carli, C., Sgavetti, M., 2015. Spectral variability of plagioclase-mafic mixtures (3): quantitatively analysis applying the MGM algorithm. Icarus 254, 34–55. https://doi.org/10.1016/j.icarus.2015.03.024.

Serventi, G., Carli, C., Sgavetti, M., 2016. Deconvolution of mixtures with high plagioclase content for the remote interpretation of lunar plagioclase-rich regions. Icarus 272, 1–15. https://doi.org/10.1016/j.icarus.2016.01.020.

Shkuratov, Y., Kaydash, V., Korokhin, V., Velikodsky, Y., Opanasenko, N., Videen, G., 2011. Optical measurements of the Moon as a tool to study its surface. Planet. Space Sci. https://doi.org/10.1016/j.pss.2011.06.011.

Sunshine, J.M., Pieters, C.M., 1998. Determining the composition of olivine from reflectance spectroscopy. J. Geophys. Res. 103, 13675–13688.

Sunshine, J.M., Pieters, C.M., Pratt, S.F., 1990. Deconvolution of mineral absorption bands: an improved approach. J. Geophys. Res. 93, 6955–6966.

Verpoorter, C., Carrère, V., Combe, J.-P., 2014. Visible, near-infrared spectrometry for simultaneous assessment of geophysical sediment properties (water and grain size) using the spectral derivative–modified Gaussian model. J. Geophys. Res. Earth Surf. 119, 2098–2122. https://doi.org/10.1002/2013JF002969.

Wiens, R.C., et al., 2021. The SuperCam instrument suite on the NASA Mars 2020 rover: body unit and combined system tests. Space Sci. Rev. (SSR) 217 (Issue: 1). https://doi.org/10.1007/s11214-020-00777-5. Article Number: 4.